Remote Host Manipulation by Pathogenic Bacterial Extracellular Vesicles

Debraj Koiri[1,3], Lydia Mathew[2‡], Ayush Panda[1‡], Divit Solanki[1], Assirbad Behura[1], Shobhna Kapoor[2], Mohammed Saleem[1,3,4*]

Affiliations

[1] School of Biological Sciences, National Institute of Science Education & Research, Bhubaneswar, India.
[2] Department of Chemistry, Indian Institute of Technology Bombay, Mumbai, India.
[3] Homi Bhabha National Institute (HBNI), Mumbai, India.
[4] Center for Interdisciplinary Sciences, National Institute of Science Education & Research, Bhubaneswar, India.
[‡] Equal contribution

[*]Correspondence: saleem@niser.ac.in

Abstract

Bacterial extracellular vesicles (BEVs) are known to enhance infection susceptibility in vivo, yet the mechanistic basis for this remote preconditioning of host cells is unknown. Here, we discover an evolutionarily conserved, lipid-driven physical mechanism by which pathogenic bacterial EVs systemically arrest phagosome maturation in bystander host cells. Using live-cell fluorescence lifetime imaging, *in vitro* reconstitution and micromanipulation we show that EVs from diverse pathogens - *Mycobacterium tuberculosis*, *Klebsiella pneumoniae*, and *Staphylococcus aureus* - fuse with host plasma, phagosomal, and lysosomal membranes. This fusion increases membrane tension and perturbs early phagosomal maturation. Transcriptomic profiling confirms a broad downregulation of phagosome maturation genes while upregulation of lysosomal stress responsive genes. Crucially, in vitro reconstitution shows that EVs, and their purified lipids alone, are sufficient to induce phase separation and increase membrane tension, directly inhibiting phago-lysosomal fusion. Our findings establish a paradigm in which pathogens exploit EVs not merely as delivery vehicles, but as tools to remotely rewire host cell membrane mechanics to hijack phagosome maturation and host defense - a strategy that moves beyond canonical effector-based models of pathogenesis.

Introduction

Phagosome maturation, a fundamental host defense mechanism, mediates pathogen degradation through phagolysosome formation [1].This involves the sequential fusion of phagosomes with lysosomes tightly orchestrated via membrane trafficking and organelle acidification [2,3]. Several pathogens have evolved sophisticated strategies to disrupt phagosome maturation, enabling their survival and replication within macrophages [4-6]. Following the initial discovery that *Mycobacterium tuberculosis* inhibits phagosome-lysosome fusion[7], numerous studies have identified the bacterial effectors responsible for this survival strategy. For example the ESX-1 secretion system [8,9], secreted lipid virulence factors[10-13] and secreted phosphatases[14,15] are all known to interfere with host signalling. An abnormal retention of early endosomal markers like Rab5 and the exclusion of late endosomal markers like Rab7 and the v-ATPase complex is also known to result in an aberrant phagosome [16]. The failure of phagosome lysosome fusion is attributed to the reduced accumulation of phosphatidylinositol-3-phosphate (PI3P) on the phagosomal membrane, which diminishes the recruitment of effector proteins essential for lysosomal fusion [17]. Mycobacterial lipids like lipoarabinomannan (LAM) and enzymes such as the phosphatases SapM and PtpA are also known to contribute to this process [18,19]. Despite decades of pursuit our understanding of the mechanism of how these effectors, particularly the Mycobacterial lipids, are trafficked to and function at the host-pathogen interface to orchestrate phagosome maturation arrest is still an intensive and unresolved area of research [20]. *Mycobacterium tuberculosis* (Mtb) secretes nanoscale extracellular vesicles (MEVs) that function as delivery vehicles, transporting a payload of bacterial lipids, proteins, and nucleic acids directly into host cells[21]. Previous research has established that these vesicles play a significant immunomodulatory role, such as by inhibiting T-cell activation [22-24]. However, the fundamental question of how MEVs interact with and alter host intracellular compartments, their precise intracellular fate and mechanism of action has remained unknown.

We discovered that pathogenic bacterial extracellular vesicles (BEVs) across bacterial kingdom (i.e, *Mycobacteriuam tuberculosis, S. aureus* and *K. pneumonia*) spontaneously fuse with the host organellar membranes and remodel their mechanical parameters. Using *Mycobacterium tuberculosis* as a primary model, we determined that extracellular vesicles upon fusion subsequently enrich their lipids in the phago-lysosomal membranes dramatically increasing the tension. This mechanical alteration delays the recruitment of the key GTPase Rab5, a master regulator that initiates phagosome maturation. This elevated membrane tension persists even after the phagosome fuses with a lysosome. Lipidomic analysis confirmed that this effect is driven by the mycobacterial extracellular vesicle (MEV)-mediated enrichment of mycobacterial lipids within host membranes, predominantly inositol derivatives like Lipoarabinomannan (LAM), Phthiocerol Dimycocerosate (PDIM), and Phosphatidylinositol Mannosides (PIMs). *In vitro* reconstitution demonstrates that the purified MEV lipid fraction is alone sufficient to increase membrane tension and drive

phase separation creating a mechanical barrier that opposes the fusion of phagosomes with lysosomes. Further, MEV lipids also elevate lysosomal membrane anisotropy evident from lifetime imaging, disrupting lysosomal homeostasis and further impairing its ability to fuse. Surprisingly, the physical manipulation of host membranes is complemented by transcriptional reprogramming of the host cell's phagosome maturation and membrane repair machinery to sustain the blocked state of maturation. Together, Our study discovers a novel, evolutionarily conserved paradigm that bacterial pathogens exploit extracellular vesicles not merely as delivery vehicles, but as tools to remotely manipulate the physical parameters of host organelle membranes, thereby hijacking a central pillar of innate immunity i.e. phagosome maturation.

Results

Mycobacterial Extracellular Vesicles (MEVs) Spontaneously Fuse With The Host Plasma Membrane

We first cultured *M.tb* H37Ra under minimal nutrient conditions to induce vesicle production. Transmission electron microscopy (TEM) revealed distinct stages of Mycobacterial extracellular vesicles (MEVs) biogenesis, including membrane protrusion and bud formation from the bacterial surface (Fig. 1A). We then isolated and purified MEVs, adopting a vesicle isolation protocol previously established for *M. tuberculosis* H37Rv [22], involving sequential differential centrifugation followed by OptiPrep density gradient ultracentrifugation. Vesicle-enriched fractions from the culture supernatants of H37Ra grown under minimal nutrient conditions revealed discrete, bilayered vesicular structures ranging from ~ 120 to 300 nm in diameter revealed by nanoparticle tracking analyzer and dynamic light scattering consistent with the known size distribution of MEVs (Fig. S1 A-C, Supplementary movie 1). Likewise, the biochemical signatures of the MEVs such as the derivatives of Lipoarabinomannan (LAM), Phthiocerol Dimycocerosate (PDIM), and Phosphatidylinositol Mannosides (PIM) were also identified using lipidomics (Fig 4B).

To visualize the initial interaction between *M.tb* H37Ra extracellular vesicles *(MEVs)* and host macrophages in real-time, PMA-differentiated THP-1 macrophages were treated with PKH67-labeled MEVs and monitored using live-cell fluorescence microscopy (Fig. S2A). Within 30 minutes of treatment, a subset of MEVs accumulated and likely fused with the macrophage plasma membrane, seen as a distinct spread of the fluorescent signal at the cell's periphery (Fig. 1B, S2A). Quantitative analysis of membrane-associated fluorescence revealed ~ 40% rise in the fluorescence intensity corresponding to docking or fusion events at the host plasma membrane (Fig. 1C). To further validate MEV - host membrane fusion, we employed a membrane fusion assay based on R18 dye fluorescence dequenching. R18 is a self-quenching lipophilic dye that exhibits increased fluorescence upon dilution in the lipid bilayer of a target membrane during fusion events [25]. R18-labeled MEVs were incubated with large unilamellar vesicles (LUVs) mimicking the host plasma membrane composition, and fluorescence intensity was monitored over time. The fluorescence of the R18 dye increased over time because the dye molecules spread out as the membranes fused (Fig. S2B). To reconfirm membrane fusion and assess lipid mixing between MEVs and host membranes, a kinetic fluorescence resonance energy transfer (FRET)-based lipid mixing assay was employed. In this assay, donor (NBD-PE) and acceptor (Rh-PE) fluorophores were incorporated into host plasma membrane-mimicking LUVs. Upon fusion with unlabeled MEVs, dilution of the donor–acceptor pair leads to a concomitant increase in donor fluorescence, indicating lipid mixing [26,27]. Consistent with the R18 dequenching results, we observed a time-dependent increase in NBD fluorescence intensity following MEV addition, suggesting that MEVs actively fuse and exchange lipids with the model host membrane (Fig. 1D). In contrast, LUVs incubated

in the absence of MEVs exhibited no appreciable change in donor fluorescence, confirming that the observed signal increase was specific to MEV-mediated fusion.

Since intensity-based FRET measurements can sometimes be prone to artifacts such as photobleaching and donor dye dilution during membrane fusion, we employed fluorescence lifetime imaging microscopy (FLIM)-FRET to more accurately assess MEV fusion. R18-labeled MEVs were incubated with NBD-PE labeled giant unilamellar vesicles (GUVs) mimicking the host plasma membrane. NBD-PE fluorescence lifetime was quantified over 40 minutes in the presence and absence of the acceptor. A significant decrease in NBD lifetime was observed in the presence of R18-labeled MEVs, indicating efficient FRET and confirming membrane fusion between MEVs and the GUVs (Fig. 1E-F). To visualize the ultrastructural intermediates of MEV fusion, we performed negative-stain transmission electron microscopy following incubation of MEVs with plasma membrane-mimicking LUVs (Fig. 1G). Distinct morphological stages of membrane fusion were observed, including initial membrane contact, hemifusion, and complete fusion. Quantitative analysis after 40 minutes of incubation revealed that approximately 70% of MEVs were at the initial contact stage, ~45% exhibited hemi fusion, and ~30% had progressed to full fusion with the LUVs (Fig. S2C). Collectively, these results indicate that spontaneous fusion of the MEVs with the plasma membrane, represents a key initial mode of interaction at the host–MEV interface.

MEV Fusion Increases the Host Plasma Membrane Tension

To assess how MEV fusion impacts membrane mechanics, we first employed fluorescence lifetime imaging microscopy (FLIM) using Flipper-TR, a molecular rotor sensitive to changes in membrane mechanical stress that quantitatively measures tension [28-31]. THP-1-derived macrophages were treated with MEVs and labelled with 100 nM Flipper-TR, and fluorescence lifetime was monitored over 40 minutes. A marked increase in probe lifetime from 4.5 ns to 4.8 ns was observed following MEV treatment, indicating a significant elevation in plasma membrane tension associated with fusion mediated reorganization (Fig. 1I,J). To validate these findings in a controlled minimal system, we used plasma membrane-mimicking GUVs doped with Flipper-TR. Consistent with the in vivo observations, MEV fusion led to an increase in lifetime from 4.6 ns to 5.0 ns (Fig. 2K,L). Regulation of cell membrane tension is essential for numerous cellular processes, including endocytosis, signalling, and vesicular trafficking[31-34]. To assess the effect of altered membrane tension on the diffusion behaviour of lipids, we monitored the fluorescence recovery after photobleaching (FRAP) of plasma membrane-mimicking giant unilamellar vesicles (GUVs) ladbelled with Atto-PE. GUVs were immobilized and incubated with MEVs for 40 minutes to allow fusion to take place, and fluorescence recovery was monitored post-bleaching (Fig. S3 A,B). In comparison to host plasma membranes, MEV-fused GUVs exhibited about ~20% lower fluorescence recovery, indicative of reduced lateral lipid diffusion. These findings suggest that MEV fusion leads to tighter lipid packing within the membrane, thereby impairing lipid mobility and altering membrane order.

These results collectively demonstrate that MEV incorporation into the membrane leads to a consistent increase in membrane tension, both in live cells and in reconstituted membranes.

To further dissect the mechanical consequences of MEV fusion on host membranes, we evaluated how MEV incorporation alters the membrane's compressibility modulus by employing Langmuir lipid monolayers. This approach enables precise measurement of the surface pressure (π) versus molecular area (A) isotherms, which reflect the thermodynamics of lipid interaction and packing density [35,36]. Plasma membrane mimicking monolayers were exposed to increasing concentrations of MEVs, and the resulting π - A isotherms were measured. We observed a significant rightward shift in the isotherms with MEV addition (Fig. S3C), suggesting that MEV integrates into the monolayer, thereby increasing the average molecular area and expanding the film.

To quantitatively assess membrane compressibility, we calculated the compressibility modulus (Cs^{-1}) from the π-A isotherms using the equation:

$$Cs^{-1} = -A\,(d\pi/dA)_t \quad (1)$$

This modulus reflects the membrane's resistance to lateral deformation. Importantly, we focused our analysis at a surface pressure range of ~30-35 mN/m, which closely mimics the lateral pressure found in biological bilayers, where lipid packing, hydrophobic free energy, and area per molecule resemble native membranes[35,36]. At this bilayer-equivalent pressure, we found that the compressibility modulus decreased significantly with increasing MEV concentration (Fig. S3D), indicating that MEV fusion renders the membrane more laterally compressible. Next, as demonstrated by the in vitro data that showed higher membrane rigidity and increased compressibility of the plasma membrane post-fusion with MEVs, we explored the effect of fusion on the cell cortical stiffness using atomic force spectroscopy. In line with in vitro assays, fusion of MEVs with PMA-differentiated THP-1 macrophages cells lead to increased elastic modulus indicative of a stiffer plasma membrane (Fig. 1H, S3E). Collectively the findings suggest a complex remodelling of the host plasma membrane in which MEV fusion enhances membrane order and stiffness in the bilayer while altering lateral lipid interactions and increasing the overall membrane tension.

MEV Fusion Triggers Actin Fragmentation And Enhanced TLR2 Expression To Increase Their Phagocytosis

To confirm the enrichment of the MEVs in the phagosome either in fused or engulfed state, PMA-differentiated THP-1 macrophages were treated with Anti-LAM antibody to detect the surface markers (i.e., LAM) on the MEV[37]. This revealed that the MEVs were efficiently internalized and fully phagocytosed within 2 hours. (Fig. 2A-B). The increase in phagocytosis of MEVs was also reflected in the rise in surface expression

of TLR2, as detected by flow cytometry (Fig. S4). We then questioned whether the the MEV internalization and fusion impacts the host cytoskeleton dynamics and their interaction with membranes to regulate the phagocytic kinetics? To investigate this, we monitored the actin network in the MEV treated macrophages. We observed an increased abundance of small actin puncta over time suggesting actin fragmentation (Fig. 2C-D). The smaller fragments of actin indicate multiple nucleating actin facilitating high rate of actin turnover essential for phagocytosis. Concomitant with actin puncta generation, quantification of actin anisotropy demonstrated that actin is more misaligned within the actin puncta observed within the cell (Fig. 2E). Anisotropic architecture is known to directly influence membrane bending [38].

Confocal and 3D iso-surface imaging revealed a time-dependent reorganisation of the actin cytoskeleton in macrophages following treatment of MEV. Under control conditions, cells displayed well-defined cortical actin and elongated filopodia, indicative of a stable, spread morphology (Fig. S5). At 2 h post treatment, actin condensation at the cell cortex becomes apparent, accompanied by a noticeable reduction in cell spreading. Quantitative analysis showed a significant increase in the volume of actin per cell area at 2 h post treatment which reduced to the level of untreated cells at later time points (Fig. S5). This suggests only a transient change in actin volume upon MEV treatment with dTHP-1 cells. Coupled with actin punctate generation, which otherwise is expected to decrease the elastic modulus, the data indicate that MEV treatment rigidifies the cell cortex (Fig. 1H). Next, we analysed tether dynamics post MEV treatment. Tethers report alterations in the membrane reservoir and curvature. While, tether force is associated with membrane stiffness, bending rigidity, and cortical interactions, tether length and number refer to changes in membrane resistance to bending. Upon MEV treatment, a decrease in tether force was observed (Fig. 2F, S6A), indicating facile pulling of tethers and hence a weaker membrane–cytoskeleton coupling. The fragmentation of actin filaments into puncta possibly remodels the interactions between the plasma membrane and the actin network. The low tether force enables high tether extension, reflected in increased tether length in dTHP-1 upon fusion (Fig. 2G). Concomitantly, as the total membrane reservoir remains the same, flow of membrane lipids to reach higher tether lengths restricts the number of tethers per cell to be formed and is observed as reduced tether number (Fig. 2H, S6B). Together, MEVs may trigger TLR2-mediated phagocytic activation, further facilitated by actin fragmentation, potentially initiating downstream phagosome formation and maturation processes.

MEVs Interfere With The Host Phagosome Maturation Pathway By Enriching Their MEV-Derived Lipids

We next investigated the impact of MEVs on phagosome maturation and to this end we tracked the recruitment dynamics of the early endosomal marker Rab5. THP-1–derived macrophages were transfected with mCherry-tagged Rab5 (mCh-Rab5),

which allowed real-time visualization of early endosome association through single-cell time-lapse imaging. Upon treatment with MEVs derived from *M. smegmatis* and *M. tuberculosis* H37Ra labelled with PKH67, Rab5 colocalization with the phagosomal membrane was significantly delayed, first appearing around 8 and 9hours post-treatment, respectively (Fig. 3B-C, Supplementary movie 4-7). This was further confirmed through maximum intensity projection images taken at end time points, which revealed Rab5 accumulation around MEV-containing phagosomes (Fig. 3B-C). In contrast, macrophages treated with *E. coli*-derived EVs showed early recruitment of Rab5 to the phagosomal membrane, with colocalization detectable as early as 3 hours post-internalization. This was visible in the maximum intensity projection images, which demonstrated robust Rab5 signal surrounding the EV-containing compartments at this earlier time point (Fig. 3A, Supplementary movie 2-3). A similar delay in Rab5 recruitment was also evident in fixed-cell imaging of macrophages expressing mCh-Rab5 at various time points post-MEV treatment, corroborating the live-cell imaging results (Fig. S7). These observations suggest that MEVs delay the recruitment of Rab5 to the maturing phagosome, potentially through spontaneous fusion with the phagosomal membrane that disrupts normal trafficking and maturation.

To further understand the molecular basis underlying the observed delay in phagosomal maturation induced by MEVs, we performed transcriptomic profiling of macrophages exposed to MEVs and compared them with untreated macrophages at different time points. RNA-sequencing analysis revealed striking transcriptional reprogramming with approximately ~ 1,000 genes differentially expressed at 12 hours relative (Fig. 3G, S8). Surprisingly, we discovered suppression of several key regulators of endosomal maturation and fusion among the genes exhibiting significant downregulation at 12 hours (Fig. 3H). These included MTM1, a phosphoinositide phosphatase critical for endosomal homeostasis[39]; Rab7B, a small GTPase that promotes transition from early to late endosomes and lysosomal biogenesis[40,41]; VAMP8, a SNARE protein required for lysosomal fusion events[42,43]; and PIKFYVE, the lipid kinase responsible for generating PI(3,5)P_2, which regulates endolysosomal trafficking and membrane dynamics [44]. The reduced expression of these factors indicates a coordinated manipulation of the molecular machinery essential for phagosome progression towards lysosomal fusion.

In contrast, several genes associated with early endosomal function and compensatory trafficking pathways were upregulated at 12 hours (Fig. 3H). These included EEA1, a canonical early endosome tethering protein that stabilizes PI(3)P-enriched membranes[45]; MCOLN1, a lysosomal Ca^{2+} channel that regulates vesicular trafficking and membrane fission events[46]; MTMR3, a phosphatase that counterbalances PI3P signaling[47]; STX8, a SNARE component linked to endosome-endosome fusion[48]; and VPS33A, a Sec1/Munc18 (SM) family protein that coordinates SNARE-mediated membrane fusion. Upregulation of these transcripts suggests that macrophages attempt to counteract MEV-induced trafficking defects by reinforcing early endosomal tethering and fusion machinery. Together, transcriptomic signatures

are in line with the delayed Rab5 recruitment and indicate an impaired lysosome-phagosome fusion. This also reveals a dual impact of MEVs on the endolysosomal system, i.e, suppression of genes essential for phagosome maturation and lysosomal fusion, coupled with compensatory upregulation of early endosomal regulators by the host (Supporting information 2).

To further investigate the effect of MEVs on phagosome-lysosome fusion, we monitored lysosomal acquisition in THP-1 - derived macrophages treated with EVs from *E. coli*, *M. smegmatis*, and *M. tb* H37Ra. Colocalization of LysoTracker, a fluorescent probe that accumulates in acidic organelles, with PKH67-labeled EV-containing compartments was monitored over time using live-cell imaging. In macrophages treated with *E. coli* EVs, robust LysoTracker colocalization was observed as early as 4 hours post-internalization, as evident from the maximum intensity projection images (Fig. 3D, Supplementary movie 8-9). In contrast, LysoTracker signal colocalization was markedly delayed in cells treated with MEVs from *M. smegmatis* and H37Ra, appearing only around 10 and 11 hours post-treatment, respectively (Fig. 3E-F, Supplementary movie 10-13). A comparable delay in phagosome-lysosome fusion was also observed in fixed-cell imaging using LysoTracker-stained macrophages at various time points following MEV treatment, further corroborating the live-cell imaging (Fig. S9). Additionally, fixed-cell imaging of THP-1 macrophages infected with *E. coli*, live GFP–*M. smegmatis*, or heat-killed *M. smegmatis*, shows lysosomal colocalization at 4 h, 48 h, and 30 h, respectively, with the pronounced delay in live *M. smegmatis* highlighting MEV-mediated impairment of phagosome–lysosome fusion (Fig. S10). These observations suggest that EVs from mycobacteria significantly delay phagosome acidification and fusion with lysosomes, further supporting their role in disrupting normal phagosome maturation pathways.

We hypothesized that the enrichment of the MEV lipid components in the phago-lysosomal membrane compartments could be responsible for the observed delay in fusion. The identification of specific lipidic changes will enable better rationalization of the changes induced in host membranes upon fusion. The lipidomic profiling of purified lysosomes, MEVs and purified lysosomes from MEV-treated macrophages was performed by extracting lipids followed by mass spectroscopy. Firstly, mycobacterial lipids identified from the MEV lipids were classified into six major lipid classes based on MtbLipidDB (i.e, glycerophospholipids, saccharolipids, glycerolipids, fatty acyls, prenols and polyketides) and in decreasing levels of abundance (Fig. 3I, Supporting information 1).

In glycerophospholipids, the predominant lipids identified were acylated versions of phosphatidylinositol mannosides (PIMs) such as AC1PIM1, AC1PIM2, AC2PIM2 and AC2PIM3 (Fig. 4A-B). These lipids are highly specific to mycobacterial species and their high abundance is mainly attributed to them being the primary membrane-forming lipids. Of note, ACPIMs are enriched within the inner plasma membrane of the cell envelope, indicating that MEVs does not explicitly contain lipids only from the outer

membrane layer. Other abundant lipids within glycerophospholipids were cardiolipins (CL), lysophosphatidylinositol (LPI), and standard phospholipids such as PA, PG, PI and PE. Within saccharolipids, the major contributors were glycopeptidolipids I and IIB among other lipid as shown in Fig 4B**.** Saccharolipids are generally known to facilitate infection and foster evasion of phagocytosis and promote membrane permeability. Mycolic fatty acids are long-chain (C60-90) fatty acids specific to mycobacterial strains and were identified in the fatty acyl lipid class (Fig. 4B) and among them, mycosanoic acid was the most abundant. We could detect both alpha and methoxy mycolic acids within the bacterial lipidome, albeit with low abundances. Next, mannosyl phosphomycoketides, and PDIM B constituted the major components within prenol and polyketides class (Fig. 4B), though their absolute abundance was low. These lipids are known to act as carrier lipids. Lipids such as mono-, di-, and tri-acyl glycerol (MAG, TAG and DAG) constituted the glycerolipids but are not selective to mycobacterial lipidome as these are also found in mammalian lipidome (Supporting information 1), and they mainly act as storage lipids. After quantifying MEV lipidome, we specifically looked for signature of mycobacterial lipids within lysosomes purified from MEV infected host cells as a result of MEV fusion. Class-wise lipid composition of untreated lysosomes is used as the baseline for comparison with MEV-fused lysosomes (Fig. 4C). As demonstrated in (Fig. 4D), we could detect all major lipids (class wise) within the fused fraction confirming membrane fusion as well as insertion of bacterial lipids within the host's lysosomal membrane. Based on these, we investigated changes within the host cellular lysosomal lipidome post integration of specific bacterial lipids which could alter membrane properties and thus influence the rate of fusion. We evaluated two main factors: alkyl chain length and degree of unsaturation. Upon fusion with MEVs, the average chain length of lipids within lysosomal membrane increased (Fig. 4E) and is mainly attributed to the integration of long-chained bacterial lipids. The dynamics of the increased chain length owing to their defective packing may contribute to free void volume resulting in disorderliness of the overall membrane. The observed decrease in degree of unsaturation (> 4 double bonds) upon fusion reflects a local ordering in the membrane (Fig. 4F). Together, we think that the fusion of MEVs though might order the membrane locally, however, hydrophobic mismatch between lysosomal and MEV lipids would induce lipid segregation leading to overall disorderliness.

MEV-derived Lipids Are Sufficient to Disrupt Lysosomal Homeostasis in Host Macrophages

Having established that MEVs fully fuse with the lysosomal compartment, we next sought to determine whether they perturb lysosomal homeostasis and which components can minimally drive the same. Alterations in key membrane biophysical properties - such as polarity, viscosity, and tension - are strongly associated with the progression of various pathological states [49-51]. Many intracellular biochemical processes are highly sensitive to local viscosity, changes in organelle-specific viscosity can serve as early indicators of cellular dysfunction [52]. To assess lysosomal

viscosity, we employed JIND-Mor, a molecular rotor-based fluorescent probe that selectively accumulates in lysosomes and reports changes in viscosity through alterations in its fluorescence lifetime [53]. Differentiated THP-1 macrophages were incubated with 0.2 μM JIND-Mor for 15 minutes before imaging, and lysosomal viscosity was monitored 12 hours post-treatment with EVs derived from *M. smegmatis* and *M. tuberculosis* H37Ra. This time point was selected based on previously observed colocalization of MEVs with lysosomes (Fig. 3E-F), ensuring that viscosity measurements reflect post-fusion lysosomal dynamics. We observed a significant increase in the fluorescence lifetime of JIND-Mor in macrophages treated with MEVs. Specifically, the average lifetime measured in cells treated with EVs from *M. smegmatis* was approximately ~3.0 ns, while EVs from *M. tuberculosis* H37Ra yielded a slightly higher lifetime of ~3.1 ns (Fig. 5A-D, E). In contrast, untreated macrophages exhibited a baseline JIND-Mor fluorescence lifetime of ~2.75 ns (Fig. 5E). This increase in fluorescence lifetime indicates an elevation in lysosomal viscosity following MEV treatment. Since JIND-Mor lifetime positively correlates with microviscosity, these results suggest that fusion of MEVs with the lysosomal membrane leads to a more viscous intra-lysosomal environment, potentially reflecting altered lipid packing or changes in luminal content dynamics. Interestingly, to delineate the specific contribution of MEV lipids to lysosomal viscosity changes, we reconstituted synthetic vesicles composed solely of lipids extracted from MEVs (hereafter referred to as MDLVs, MEV-derived lipid vesicles), maintaining a size distribution comparable to native MEVs. Upon treating macrophages with these MDLVs and subsequently monitoring lysosomal viscosity using JIND-Mor, we observed a striking increase in fluorescence lifetime, reaching approximately ~3.4 ns (Fig. 5D-E). This enhancement exceeds that observed with intact MEVs, indicating that the lipid components alone are sufficient to induce significant alterations in lysosomal microviscosity.

Lysosomal membrane order (or fluidity) is a critical factor in maintaining lysosomal homeostasis and function [54]. To assess how MEVs influence lysosomal membrane dynamics, we quantified fluorescence anisotropy of JIND-Mor localized to the lysosomal membrane, extrapolating data from Fig. 5A-E. Compared to untreated macrophages, which displayed a baseline anisotropy of ~0.073 (Fig. 5F, J), MEV-treated cells exhibited a marked reduction in lysosomal membrane anisotropy. Specifically, macrophages treated with MEVs from *M. smegmatis* showed an average anisotropy of ~0.032, while treatment with MEVs from *M. tuberculosis* H37Ra yielded a slightly higher value of ~0.038 (Fig. 5G-H, J). These results indicate a significant membrane disorderliness upon MEV fusion. Consistent with this, macrophages treated with MDLVs composed solely of MEV-derived lipids also demonstrated a decreased anisotropy of ~0.034 (Fig. 5I-J). To confirm this further, we isolated and purified the lysosomes as described [54] from MEV-treated and MDLV-treated macrophages and found the fluorescence anisotropy of DPH to decrease by ~ 4% (Fig. 5K). Membrane tension is essential for fusion–fission dynamics and maintenance of organelle integrity, thereby playing a pivotal role in cellular homeostasis[34-37]. To investigate whether MEVs modulate lysosomal membrane

tension, we employed the lysosome-targeted mechanosensitive probe Lyso-Flipper. Untreated macrophages exhibited a baseline Lyso-Flipper fluorescence lifetime of ~4.7 ns (Fig. 5L). Upon treatment with MEVs derived from *M. smegmatis*, the lifetime increased to ~4.85 ns, while MEVs from *M. tuberculosis* H37Ra produced a similar increase to ~4.98 ns. Notably, MDLVs also elevated the lysosomal membrane tension, with a lifetime of ~4.8 ns (Fig. 5 L-P). This suggests that MEVs and specifically their lipid constituents are sufficient to induce measurable increases in lysosomal membrane order and tension, potentially contributing to altered lysosomal mechanics and disrupted homeostasis.

We next asked whether these changes translate into transcriptional reprogramming of host macrophages. To address this, we performed RNA sequencing of untreated and MEV-treated macrophages at different time intervals. At the 12-hour post treatment, MEV exposure induced a broad transcriptional response with approximately 300 genes differentially expressed compared to untreated macrophages (Fig. 5Q). Pathway enrichment analysis of these early transcriptional changes revealed significant enrichment in categories associated with lysosomal stress, lysosomal membrane damage and lipid metabolic processes, consistent with the cellular response to altered membrane homeostasis (Fig. 5Q). However, 24 hours post-treatment, the transcriptional profile consolidated into a focused set of genes strongly linked to lysosomal function and stress signaling. We observed marked upregulation of cathepsins (*CTSD*, *CTSL*, *CTSB*), reflecting an attempt to enhance proteolytic activity in response to impaired lysosomal degradation (Fig. 5R). In addition, *LGALS3* (Galectin-3), a known sensor of lysosomal membrane damage [55], was significantly upregulated, indicating the engagement of damage surveillance pathways. Importantly, *TFEB* the master regulator of lysosomal biogenesis and autophagy[56] was also upregulated, suggesting the initiation of a compensatory transcriptional program to restore lysosomal capacity (Fig. 5R).

Interestingly, several genes central to lysosomal integrity and lipid homeostasis were downregulated (Fig. 5R). These included *GBA2* (β-glucosidase 2), a key enzyme in glycosphingolipid metabolism [57]; *CHMP4B*, a component of the ESCRT-III complex essential for membrane repair and intraluminal vesicle formation [31]; and *SMPD1*, encoding acid sphingomyelinase, which regulates membrane curvature and lipid turnover [58]. The suppression of these genes suggests that MEV-derived lipids may impair the cell's ability to restore lysosomal stability and lipid balance, thereby compounding the mechanical stress imposed at the membrane level. Together, these transcriptomic findings reveal that MEV-induced alterations in lysosomal membrane mechanics are paralleled by activation of lysosomal stress-adaptive programs (cathepsins, TFEB, galectins) and simultaneous suppression of repair pathways. This transcriptional dichotomy suggests that while macrophages attempt to compensate for lysosomal dysfunction, MEV-derived lipids create a sustained imbalance that prevents effective restoration of lysosomal homeostasis (Supporting information 2).

MEV-derived Lipids Elevate Host Phagosomal Membrane Tension to Inhibit Phagosome–Lysosome Fusion

We next sought to determine whether the inhibition of phagosome–lysosome fusion correlates with the membrane remodeling induced by MEV-derived lipids. To address this, using micropipette aspiration, we quantified the change in tension of GUV membrane doped with MEV-derived lipids in comparison to GUVs mimicking native phagosomal membrane. Notably, MEV-lipid-doped membranes displayed markedly higher thermal membrane fluctuations compared to native phagosomal membranes. During aspiration, the vesicle geometry - specifically the aspiration length (*Lp*) and vesicle radius (*Rv*) (Fig. 6A-B, Supplementary movie 14-15) was monitored to assess changes in membrane mechanics. Under a constant applied pressure (Fig. 6A-B), MEV-lipid-doped membranes exhibited a significantly greater aspiration length (*Lp*) relative to control membranes, indicating enhanced membrane tension (Fig. 6C). Quantitative analysis revealed that MEV-lipid incorporation reduced the area stretch modulus by approximately ~ 1.5-fold compared to control membranes (Fig. 6D). Similarly, the bending modulus of the host membrane decreased by nearly tenfold in the presence of MEV-derived lipids (Fig. 6E) . For vesicles where *Lp* = 0, no direct area expansion occurred, preventing the determination of both area stretch modulus and bending modulus. To further validate these observations, we performed fluorescence lifetime imaging using the mechanosensitive probe Flipper-TR (Fig. 6F-G). Phagosomal membrane mimicking GUVs and their MEV-lipid–doped counterparts were prepared with varying molar percentages of MEV lipids and labelled with Flipper-TR. Consistent with the previous observations, MEV-derived lipids induced a concentration-dependent increase in fluorescence lifetime, indicative of elevated membrane tension (Fig. 6G).

To determine whether membrane tension directly influences Rab5 recruitment onto the phagosomal membrane, we used THP-1–derived macrophages stably expressing mCherry-tagged Rab5 (mCh-Rab5) and monitored endocytic trafficking through single-cell time-lapse imaging. Cells were pulsed with 70-kDa fluorescent dextran for 20 minutes to label newly formed endocytic vesicles, after which imaging was initiated under controlled osmotic environments to modulate membrane tension. Under isotonic conditions, where membrane tension remains close to physiological levels, Rab5 recruitment onto dextran-containing endosomes was detected within ~30 minutes. In hypertonic conditions, which reduce membrane tension by causing cellular shrinkage, Rab5 was recruited even earlier within ~20 minutes indicating that a relaxed membrane facilitates early endosomal maturation. In striking contrast, under hypotonic conditions, where cells experience membrane stretching and elevated membrane tension, Rab5 recruitment was completely abolished, and no detectable association of Rab5 with endosomal membranes occurred till ~40 minutes (Fig. 6I).These results demonstrate that increased membrane tension impairs early endosomal maturation by blocking Rab5 recruitment, while reduced tension accelerates the process, highlighting membrane tension as a key biophysical regulator of phagosomal

progression. This suggests that fusion of MEVs with the phagosomal membrane markedly elevates membrane tension, which in turn hampers the recruitment of Rab5 to the membrane (Fig. 3 B-C).

Interestingly, doping the phagosomal membrane with MEV-derived lipids triggered pronounced liquid–liquid phase separation within the bilayer, a process intrinsically linked to changes in membrane line tension (i.e, the free energy per unit length of the interface between coexisting lipid phases). To investigate this effect, we reconstituted giant unilamellar vesicles (GUVs) mimicking the phagosomal lipid composition and incorporated with 25 mol% mycobacterial lipids (Fig. 7A, Supplementary movie 16-17, S11). The vesicles were co-labelled with TopFluor Cholesterol (Lo phase marker, green) and Rhodamine-PE (Ld phase marker, red) to visualise lateral membrane heterogeneity. Through time-lapse Confocal top-view imaging revealed that well-defined *Lo* and *Ld* domains in lipid-doped GUVs. These domains were separated by sharply delineated boundaries, consistent with high *Lo–Ld* interfacial energy. Over time, the domains underwent coarsening, driven primarily by domain coalescence (fusion of adjacent like-phase domains). Both processes are thermodynamically favoured when line tension is high, because the system minimizes total boundary length to reduce the interfacial free energy. From a biophysical perspective, the line tension (γ) at the domain boundary can be described as:

$$\gamma = \frac{\Delta G_{boundary}}{L}$$

Where, $\Delta G_{boundary}$ is the excess free energy associated with the phase boundary and L is the boundary length. Increased γ drives the system toward larger, fewer domains, as observed here. In contrast, control GUVs mimicking native phagosomal membranes without MEV-derived lipids displayed uniform fluorescence, indicating the absence of phase separation and negligible line tension under identical imaging conditions. Taken together, these findings suggest that MEV-derived lipids increase *Lo–Ld* interfacial energy, resulting in higher line tension. This physical change promotes domain growth, stabilizes large-scale lateral heterogeneity, and could increase the energetic barrier for membrane mixing, providing a plausible mechanism for MEV-mediated inhibition of phagosome–lysosome fusion. We then wondered whether lysosomes undergo phase separation inside cells? To check this, we purified lysosomes from uninfected as well as MEV infected macrophage. Negative staining transmission electron microscopy revealed a striking difference between the two pools of purified lysosomes (Fig. 7 B-C). The lysosomes purified from uninfected cells showed a clear distinct circular boundaries with a sharp contrast. On the contrary, the lysosomes purified from infected cells showed discontinues boundaries without collapsing membranes either as distinct compartments or two compartments in a fused states. These observations reflect that the MEV fused lysosome either undergo phase separation or lysis.

Finally, to assess the functional consequence of this mechanically altered state, we examined phagosome-lysosome fusion using a Förster Resonance Energy Transfer (FRET)-based lipid mixing assay (Fig. 7D). Phagosome-mimicking liposomes containing 0, 10, or 25 mol% MEV-derived lipids were mixed with lysosome-mimicking liposomes at a 1:3 molar ratio (lysosome: phagosome) in the presence of 10% (w/v) PEG to simulate cytosolic crowding. In control vesicles, robust lipid mixing was observed, reflected in high FRET efficiency between donor (NBD) and acceptor (Rhodamine) fluorophores. MEV-lipid incorporation caused a dose-dependent reduction in FRET efficiency, accompanied by recovery of donor fluorescence, indicating impaired membrane fusion. The most pronounced inhibition occurred at 25 mol%, correlating with the strongest mechanical alterations. Together, these data suggest that MEV-derived lipids remodel the phagosomal membrane by increasing tension thereby reducing its fusogenic potential with lysosomes (Fig. 7E).

EVs from diverse bacterial species induce conserved membrane remodelling and impair phagosome maturation

To determine whether EV-induced membrane remodelling is conserved across bacterial species, we extended our analysis to extracellular vesicles derived from *Klebsiella pneumoniae* (KEVs; Gram-negative) and *Staphylococcus aureus* (SEVs; Gram-positive). THP-1-derived macrophages treated with SEVs or KEVs were labelled with the mechanosensitive probe Flipper-TR (100 nM), and membrane mechanics were monitored by fluorescence lifetime imaging microscopy (FLIM). Time-resolved measurements over 60 min revealed a rapid and significant increase in Flipper-TR lifetime following EV exposure. KEV treatment increased the lifetime from ~4.5 ns to ~5.7 ns, while SEV treatment increased it from ~4.6 ns to ~5.4 ns (Fig. 8A-D), indicating a pronounced elevation in host membrane tension induced by EVs from both Gram-negative and Gram-positive bacteria.

We next examined the kinetics of phagosome–lysosome fusion for EVs from these species. Live-cell imaging showed that KEV-containing phagosomes acquired lysosomal markers at ~4 h post-internalisation (Fig. 8E), whereas fusion of SEV-containing phagosomes occurred slightly later, at ~5 h (Fig. 8F). To test whether EV-derived lipids remodel phagosomal membranes in a manner that could influence fusion efficiency, we reconstituted phagosomal membrane mimics doped with 25 mol% KEV- or SEV-derived lipids and monitored lateral membrane organization. KEV-lipid–doped membranes developed clear phase-separated domains after ~6 h, whereas SEV-derived lipids induced rapid phase separation within ~1 h (Fig. 8G-H). The emergence of these coexisting membrane phases is consistent with increased line tension at domain boundaries, accompanied by elevated membrane tension.

Finally, we assessed whether EV fusion perturbs lysosomal membrane mechanics. Using the lysosome-targeted mechanosensitive probe Lyso-Flipper, we observed a significant increase in fluorescence lifetime upon EV fusion, reaching ~4.7 ns for KEVs and ~4.85 ns for SEVs (Fig. 8I-L). These data indicate elevated lysosomal membrane tension induced by EVs from both species. Collectively, these findings demonstrate that EVs from diverse bacteria induce conserved remodelling of host and lysosomal membranes, generating mechanically stressed compartments that are less permissive to efficient phagosome–lysosome fusion and thereby disrupting lysosomal homeostasis.

Discussion

Our study identifies Bacterial Extracellular Vesicles (BEVs) as an evolutionarily conserved tools in hijacking phagosome maturation. Using Mycobacteria as a model we first discover that MEV fusion, and notably, MEV-derived lipids alone, is sufficient to remodel the host's plasma, endosomal and lysosomal membranes by increasing membrane tension, stiffness, and line tension**.** Such manipulation of host membrane physical parameters, though subtle in magnitude, may have striking functional consequences for intracellular trafficking[59,60]. The modulation of membrane tension is known to impact the clathrin-mediated endocytosis as well as intra-luminal vesicle formation and endosome trafficking [31,34].

Using a quenching-based assay in vivo, supported by FRET and FLIM-FRET in reconstituted systems, we first established that MEVs spontaneously fuse with the host plasma membrane elevating its membrane tension and stiffness (Fig. 1). Mycobacterial virulence lipids such as phthiocerol dimycocerosates, trehalose dimycolate and sulfolipids upon exogenous treatment with cells are known to perturb host signaling by altering the order and stiffness in the plasma membrane [61-64]. However, these minimalist yet elegant studies bypassed the critical question of how these inherently hydrophobic molecules are delivered to their intracellular membrane targets during a natural infection, including the delivery mechanism, dosage, and specific intracellular targeting of these hydrophobic effectors. Our study provides the critical missing link by identifying MEVs as physiological delivery system enabling spatially distributed enrichment of complex envelope lipids and tuning of host membranes. The increased tension of the phagosomal membrane delays the critical recruitment of Rab5 (Fig. 3, 6 & 7), an essential GTPase that governs early endosome maturation[5]. Indeed marked increase in the phagosomal membrane tension is expected to alter the lipid packing defects that can impact the Rab binding[65,66], thus delaying the limiting step for phagosome maturation. Mycobacteria are known to escape out into the host cytosol after rupturing the phagosome by the secretion of virulence factors such as ESAT-6[9,36] and continue to secrete the MEVs in the host cytosol [22]. We find that MEV lipids such as derivatives of LAM, PDIM, PIM, and Mycolactone enrich in lysosomes, increasing the lysosomal membrane tension and viscosity (Fig. 4 & 5). The enrichment of MEV-derived lipids in the lysosomal membranes results in phase separation and accumulation of line tension at the boundaries owing to the hydrophobic mismatch that can trigger lysis [67]. Interestingly, the purified lysosomes from the MEV infected cells seem to show a population of both phase separated and lysed lysosomes suggesting lysophagy. The increase in lysosomal viscosity and tension induced by MEV lipids could compromise degradative capacity, nutrient recycling, and signalling from lysosomal platforms such as mTORC1 (Fig. 5) [56]. This mimics the lysosomal dysfunction and metabolic stress reported during live *Mycobacterium tuberculosis* infection [68], suggesting that MEV cargo alone can recapitulate core aspects of bacterial virulence thus hijacking not only the pathogen containing host but also bystander cells. The trafficking of MEV lipids to lysosomes

prompted us to investigate the fate of early phagosomal compartments. Quantification of membrane tension for early phagosomal compartments is limited by the lack of probes and direct measurements, thus, we resorted to reconstituting phagosomal compartment enriched with MEV-derived lipids *in vitro*. Indeed quantitative measurement by lifetime, time-lapse imaging and micropipette aspiration showed a marked increase in membrane tension and line tension as a function of increasing amounts of MEV-derived lipids enrichment (Fig. 6). Importantly, our FRET-based lipid mixing assay established a direct link between MEV lipids and fusion inhibition. Incorporation of 10–25 mol% MEV lipids into phagosome-mimicking liposomes significantly reduced fusion efficiency with lysosome-mimicking vesicles (Fig. 7). This block correlated with the increased membrane tension detected by FLIM-Flipper-TR measurements, consistent with the principle that elevated tension and line tension increase the energetic barrier for hemifusion and pore opening[33,69,70]. Thus, MEV lipids act as mechanical inhibitors of fusogenicity, rewiring the phagosomal membranes to resist lysosomal fusion.

A striking transcriptional reprogramming of the host reinforces the organelle-wide mechanical rewiring. RNA-seq of MEV-infected macrophages revealed suppression of key phagosomal maturation genes (*Rab7, Syntaxin, VAMP8*) and upregulation of lysosomal stress (*CTSD, CTSL, LGALS3*) and membrane repair (*CHMP4B*) markers. This indicates there is a tug-of-war situation between the MEV induced manipulation and the host response to counter it. Plasma membrane tension is known to activate mTORC2 and PLD pathway [29,71], that in turn regulates the expression of TFEB, a master regulator of lysosomal biogenesis. RNA seq data for MEV infected macrophage indicates an upregulation of both mTORC2 and PLD genes and downregulation of TFEB causing the delay. Thus, we propose that MEV mediated rise in the host membrane tension reprograms host transcription machinery of phagosome maturation via mTORC2/PLD - TFEB axis.

Surprisingly, extracellular vesicles of *S. aureus* and *K. pneumonia* were also observed to delay phagosome maturation by altering the tension of cellular membranes (Fig. 8). This establishes bacterial EVs an evolutionary conserved mechanism that enable pathogens to hijack host and bystander cells through mechanical, rather than solely biochemical, manipulation remotely. By delivering a lipid cargo that alters tension, viscosity, line tension across phagosome and lysosome, bacterial EVs create an energy barrier that blocks phago-lysosomal fusion and disrupts homeostasis (Fig. 9). This dual mode of inhibition provides a powerful survival advantage to the bacterium by preventing phagosomal maturation at the site of entry, but also renders lysosomes intrinsically less competent to fuse with incoming phagosomes. This reveals a broader paradigm in pathogenesis - the exploitation of host membrane mechanics via extracellular vesicles provides a potent, lipid-driven generic strategy to subvert cellular processes, complementing the protein-based effectors.

Material and method

Materials

1,2-dioleoyl-*sn*-glycero-3-phosphocholine (DOPC), 1,2-dioleoyl-*sn*-glycero-3-phosphoethanolamine (DOPE), BSM, di-stearoyl phosphatidyl ethanolamine-PEG (2000)-biotin and cholesterol were purchased from Avanti Polar Lipids. Fluorescent conjugated lipid lissamine rhodamine B sulfonyl (Liss Rhod PE) was also purchased from Avanti Polar Lipids. Avidin coated on the chamber slides was purchased from Sigma-Aldrich.PKH-67 dye used to label MEVs procured from Sigma-Aldrich. Roswell Park Memorial Institute medium (RPMI-1640), 1× Dulbecco's phosphate buffer saline (D-PBS), sodium bicarbonate, 20× antibiotic–antimycotic solution, amphotericin-B, streptomycin, penicillin, paraformaldehyde, PMA (phorbol 12-myristate-13-acetate), were purchased from Sigma-Aldrich.

Mammalian cell culture

THP-1 monocytes were cultured in Roswell Park Memorial Institute (RPMI) 1640 medium (Gibco) supplemented with 10% fetal bovine serum (FBS) and maintained to confluence in a 5% CO_2 incubator. Cells were seeded onto appropriate culture dishes and differentiated into macrophages using 50 ng/mL phorbol 12-myristate 13-acetate (PMA; Sigma-Aldrich). After 24 h of PMA treatment, the medium was replaced, and cells were allowed a 24 h resting phase before experiments. These cell lines were not re-authenticated in our laboratory. For overexpression experiments, differentiated THP-1 macrophages were transfected with the respective constructs using Lipofectamine LTX (Invitrogen) following the manufacturer's protocol. For LysoTracker assays, cells were incubated with 70 nM LysoTracker Red (Invitrogen) for 30 min before imaging.

Mycobacteria and bacterial culture

Mycobacterium tuberculosis (*Mtb*) H37Ra (avirulent), M. smegmatis were cultured in minimal medium (MM) containing 1 g L^{-1} KH_2PO_4, 2.5 g L^{-1} Na_2HPO_4, 0.5 g L^{-1} asparagine, 50 mg L^{-1} ferric ammonium citrate, 0.5 g L^{-1} $MgSO_4 \cdot 7H_2O$, 0.5 mg L^{-1} $CaCl_2$, and 0.1 mg L^{-1} $ZnSO_4$, supplemented with 0.1% (v/v) glycerol (pH 7.0) and with or without 0.05% (v/v) tyloxapol. In certain experiments, cultures were maintained in Middlebrook 7H9 (M7H9) broth supplemented with 10% (v/v) oleic acid–albumin–dextrose–catalase (OADC; BD Microbiology Systems) and 0.5% (v/v) glycerol. Cultures were incubated at 37 °C for up to 10 days before vesicle isolation. Cell viability at day 10 was quantified by enumerating colony-forming units (CFUs) obtained from serial dilutions plated on Middlebrook 7H11 agar.

Isolation and purification of Mycobacterial Extracellular Vesicles (MEV)

Extracellular vesicles were isolated as previously described [22] with minor modifications to enhance yield and purity. Briefly, 1 L bacterial cultures were harvested by centrifugation at 3,450 × g for 15 min at 4 °C, and the cell-free supernatants were passed through 0.45 µm polyvinylidene difluoride (PVDF) filters (Millipore) to remove residual cells. Filtrates were concentrated ~20-fold using an Amicon Ultrafiltration System (Millipore) equipped with a 100 kDa molecular weight cut-off membrane. The concentrate was sequentially centrifuged at 4,000 × g and 15,000 × g for 15 min each at 4 °C to remove remaining cell debris and aggregates. Vesicles were then pelleted by ultracentrifugation at 100,000 × g for 1 h at 4 °C. The crude vesicle pellet was resuspended in 1 mL of 10 mM HEPES (pH 7.4) containing 150 mM NaCl, and mixed with 2 mL of 35% (w/v) OptiPrep solution (Sigma–Aldrich) prepared in the same buffer. This suspension was overlaid with a discontinuous OptiPrep density gradient (30–35% w/v) and centrifuged at 100,000 × g for 16 h at 4 °C. Following centrifugation, 1 mL fractions were collected from the top of the gradient, dialyzed individually against PBS overnight at 4 °C, and recovered by ultracentrifugation (100,000 × g, 1 h, 4 °C). Purified vesicles were finally resuspended in PBS and stored at 4 °C for immediate use. Vesicle size distribution and polydispersity were determined by dynamic light scattering (DLS).

Nanoparticle Tracking Analysis (NTA)

The size distribution and concentration of isolated membrane vesicles were determined using Nanoparticle Tracking Analysis (NTA, Malvern Panalytical) at 405nm. Vesicle samples were diluted 100-fold in sterile phosphate-buffered saline (PBS) to achieve optimal particle concentration for measurement.PBS alone was used as a negative control to ensure the absence of particulate contaminants and validate instrument performance. NTA provided quantitative data on vesicle size distribution and particle number in the stock solution, confirming the homogeneity and quality of the extracted vesicles.

Light Microscopy

Eight-well chambered slides (Ibidi) were coated with 10 µL of 1 mg/mL streptavidin, followed by the addition of 200 µL of biotinylated GUVs. The slide was incubated for 15 min to allow immobilization of the GUVs. MEVs were then added into the chamber. Imaging was performed on an Olympus FV3000 confocal microscope using the appropriate excitation lasers. Identical laser power and detector gain settings were maintained for all experimental conditions.

Fluorescence Recovery After Photobleaching (FRAP)

For FRAP measurements, GUVs were doped with 0.1% Atto-PE and incubated with MEVs for 1 h to allow efficient fusion. Pre-bleach images were acquired at reduced laser intensity. Photobleaching of the selected ROI was performed at full laser power

for 30 s at the equatorial plane of the GUV. After bleaching, the laser intensity was returned to the attenuated setting and fluorescence recovery was recorded over time. FRAP measurements for each condition were repeated three times, and recovery curves were normalized before analysis.

Preparation of GUV

Giant unilamellar vesicles (GUVs) were formulated to mimic the lipid composition of the phagosomal membrane, comprising 40 mol% 1,2-dioleoyl-sn-glycero-3-phosphocholine (DOPC), 5.5 mol% 1,2-dioleoyl-sn-glycero-3-phosphoethanolamine (DOPE), 22 mol% brain sphingomyelin (BSM), 32.5 mol% cholesterol, 0.03 mol% 1,2-distearoyl-sn-glycero-3-phosphoethanolamine–polyethylene glycol–biotin (PEG–biotin), and 0.1 mol% Lissamine Rhodamine PE (Rhod–PE). GUVs were generated via electroformation as described previously[36], with modifications to optimize yield. Briefly, 15 μL of the lipid mixture (5 mg mL^{-1} in chloroform) was uniformly deposited onto indium–tin–oxide (ITO)-coated glass slides (Nanion Technologies GmbH) and dried under vacuum for ≥2 h to remove residual solvent. The resulting lipid film was rehydrated in phosphate-buffered saline (PBS, pH 7.4; 300 ± 5 mOsm) and subjected to electroformation under a sinusoidal AC field (2 V, 10 Hz) at 60 °C for 3 h to promote GUV growth.

R18 dequenching (lipid mixing) fluorescence assay

For R18 labelling of MEVs, MEVs were fluorescently labelled using Octadecyl Rhodamine B chloride (R18 dye). A total of 0.6 μL of R18 (optimised concentration) was added to the MV suspension and sonicated in a water bath sonicator for 30 min, with alternating cycles of 3 min sonication followed by 5 min rest to achieve uniform dye incorporation under a highly quenched state. Unbound dye was removed using G-50 MicroSpin columns (Cytiva, Cat. No. 27533001). The columns were first centrifuged for 3 min to remove the storage buffer and compact the resin. 100 μL of R18-labelled vesicles were then carefully loaded onto the column and centrifuged at 450 × g for 3 min. The eluate containing purified R18-labelled MVs was collected for subsequent use.

The R18 dequenching assay was performed to monitor the membrane fusion kinetics of MEVs as previously described [28]. Fusion-induced dilution of the self-quenching dye R18 increases in fluorescence intensity. R18-labelled MEVs were mixed with unlabeled plasma membrane–mimicking liposomes (DOPC/DOPE/SM/Chol) at a 1:9 molar ratio in PBS (pH 7.4). Fluorescence emission at 595 nm was recorded over time using a spectrofluorometer (excitation: 545 nm; slit width: 5 nm for both excitation and emission).

The percentage of membrane fusion was calculated using the following equation:

$$\text{Fusion (\%)} = \left(\frac{F_t - F^0}{F\alpha - F^0}\right) * 100$$

where F_0 is the fluorescence at time zero, F_t is the intensity at time t, and Fα represents the maximum fluorescence obtained after adding Triton X-100 to fully disrupt the membranes and achieve infinite dye dilution.

For cellular fusion assays, the fusion efficiency of MVs with host cells was assessed using differentiated THP-1 macrophages. Purified R18-labelled MVs were added at an optimized ratio of 200 vesicles per cell. Membrane fusion was quantified by monitoring R18 fluorescence dequenching, which reflects dilution of the self-quenching dye upon fusion of the labelled vesicles with the host cell membrane.

Forster Resonance Energy Transfer-based lipid mixing assay

Fusion between plasma membrane–mimicking LUVs and MEVs was quantified by monitoring changes in FRET efficiency between NBD-PE (donor) and Rh-PE (acceptor). Lipid-mixing kinetics were assessed by measuring donor fluorescence dequenching over time, reflecting dilution of the FRET pair upon fusion. Probe-containing LUVs were mixed with probe-free vesicles at a 1:9 ratio, maintaining a total lipid concentration of 200 μM. Donor emission was recorded at 530 nm (excitation: 465 nm) for 4 h using a CLARIOstar microplate reader.

For phagosome–lysosome FRET assays, fluorophores were incorporated into lysosomal membranes, and donor fluorescence changes were monitored following interaction with phagosomes containing varying molar percentages of MEV-derived lipids. All experiments were performed in PBS (pH 7.4) at 37 °C.

Lipid Monolayer experiments

Monolayer measurements were conducted using a KSV NIMA Langmuir balance equipped with two movable barriers and a Wilhelmy plate microbalance (filter paper plate) for surface pressure detection. Lipid monolayers composed of DOPC:DOPE:SM:Chol were prepared by spreading a lipid–chloroform solution (1 mg mL^{-1}) dropwise onto the autoclaved and filtered double-deionized water maintained at 25 °C. After spreading, the monolayers were allowed to equilibrate for 15 min to enable complete solvent evaporation. For membrane conditions incorporating MEV lipids, the lipids were added to the monolayer mixture at increasing molar percentages. Surface pressure–area (π–A) isotherms were recorded during symmetric compression of the monolayer at a constant barrier speed of 1 mm min^{-1} until the collapse pressure (πc) was reached. The Langmuir trough was thoroughly cleaned before each experiment by sequential rinsing with ethanol and filtered double-deionized water until the surface pressure returned to zero. All experiments were performed in triplicate.

Micropipette Aspiration

Micropipette aspiration experiments were performed on an Olympus IX83 epifluorescence microscope (100× objective) equipped with Hoffman modulation contrast optics. Three-axis hydraulic micromanipulators were used to precisely position the micropipette. Borosilicate glass capillaries (10 μm inner diameter) were pulled using a Narashige Micro Forge MF-900 and Sutter Instruments P-87 puller to generate micropipettes. Approximately 100 μL of GUV suspension was deposited on a coverslip for analysis.

A controlled suction pressure (ΔP) was applied to aspirate vesicles into the pipette, generating a uniform membrane tension (τ) given by:

$$\tau = \frac{1}{2} * \frac{R_{\text{pipette}} \Delta \text{P}}{1 - (R_{\text{pipette}}/R_{\text{GUV}})}$$

where R_{pipette} and R_{GUV} represent the radius of the pipette and GUV, respectively.

The projection length (Lp) inside the pipette was monitored to quantify membrane area changes. The apparent area increase (Δa) was calculated using:

$$\Delta \text{a} = 2\pi R_{\text{pipette}}\, \Delta \text{Lp} + 2\pi R_{\text{pipette}}^2$$

The reference area (a_0) for a spherical vesicle was defined as:

$$a_0 = 4\pi R_{GUV}^2$$

The areal strain was thus determined by:

$$\Delta a/a_0 = R_{pipette}^2(1 + L_p/R_{pipette})/2R_{GUV}^2$$

Changes in Lp with varying ΔP were recorded (Fig. 4d). Membrane area expansion was analyzed over a tension range of 76–550 μN/m (Fig. 4e). The area stretch modulus (K_a) was obtained from the slope of the τ–Δa plot, while the bending modulus (K_b) was determined from the slope of the semi-log(τ)–Δa plot. All measurements were performed at room temperature.

Transmission Electron Microscopy

Negative staining was performed as previously described[36], with minor modifications. Briefly, purified MEVs (10 μL) were adsorbed onto carbon-coated copper grids for 40 min and excess liquid was removed using qualitative filter paper (Himedia). Grids were fixed with 10 μL of 2.5% (v/v) glutaraldehyde, rinsed with deionized water, and subsequently stained with 10 μL of 2% (w/v) uranyl acetate for 3 min. After an

additional rinse with deionized water, grids were vacuum-dried overnight. TEM imaging was performed using a JEOL JEM-2100F transmission electron microscope. For vesicle–vesicle fusion assays, MEVs and large unilamellar vesicles (LUVs) were co-incubated on carbon-coated grids before fixation and staining, following the same procedure described above.

TLR-2 Surface staining and Flow cytometry

Surface staining was performed as previously described[72], with minor modifications. Briefly, THP-1 cells were seeded in 6-well plates and differentiated into macrophages by treatment with phorbol 12-myristate 13-acetate (PMA) for 12–14 h. Differentiated cells were washed and blocked with 1% BSA for 30 min at 4 °C to prevent nonspecific antibody binding. Cells were then incubated with primary antibodies against TLR2 for 30 min at 4 °C, followed by staining with Alexa Fluor 488–conjugated secondary antibodies for an additional 30 min at 4 °C in the dark. After staining, cells were washed with FACS buffer (1× PBS supplemented with 1% BSA and 0.01% NaN_3) and immediately analyzed by flow cytometry.

Fluorescence Lifetime Imaging Microscopy (FLIM)

Fluorescence lifetime imaging microscopy was performed on an MT200 time-resolved confocal microscope (PicoQuant, Berlin, Germany) equipped with a time-correlated single-photon counting (TCSPC) unit. Excitation was provided by a 488 nm and 519 nm pulsed laser was used as per the experimental requirement, with power adjusted between 10–100 nW (measured post-dichroic). Samples were mounted in glass-bottom wells positioned on a 60× water-immersion objective. A 488 nm and 519 nm dichroic mirror served as the main beam splitter as per the flurophore. Out-of-focus fluorescence was rejected using a 50 µm pinhole, and in-focus emission was split by a 50/50 beam splitter into two detection paths. Fluorescence photons were detected by single-photon avalanche diodes (SPADs). Data acquisition and lifetime analysis were performed using SymPhoTime 64 software (PicoQuant GmbH, Berlin, Germany). For plasma Membrane tension quantification assays, 100nM of Flipper-tr were incubated for 30 minutes before imaging. For lysosomal membrane tension quantification, 1µM of Lyso-flipper was incubated for 15 minutes before imaging.

Fluorescence Lifetime Imaging Microscopy (FLIM) - FRET

For FLIM–FRET measurements, NBD was used as the donor and R18 as the acceptor. Donor excitation was carried out at 488 nm, and emission was collected above 519 nm, with R18 emission spectrally excluded to ensure single-channel donor lifetime detection. Donor-only (NBD-labeled) and donor–acceptor (NBD+R18) samples were imaged under identical acquisition settings. All measurements were conducted at room temperature, with at least three independent biological replicates.

Immunofluorescence Staining of Internalised MEVs

THP-1–derived macrophages (5 × 10^4 cells per coverslip) were seeded onto sterile glass coverslips. Following MEV treatment, cells were gently rinsed with 1× PBS and fixed with 4% paraformaldehyde (PFA; Thermo Fisher Scientific) for 20 min at room temperature. Excess fixative was removed by three washes with 1× PBS (5 min each). Cells were permeabilised with 0.1% Triton X-100 for 10 min and blocked with 1% BSA for 1 h at room temperature. For detection of internalised MEVs, cells were incubated overnight in a humidified chamber with anti-LAM primary antibody (Thermo Fisher; 1:50 in blocking buffer). After three washes with 1× PBS, Alexa Fluor 488–conjugated anti-rabbit secondary antibody (Invitrogen) was applied for 45 min in the dark. Samples were washed three additional times with 1× PBS, and coverslips were mounted for imaging.

Lysosomal purification

THP-1 cells were cultured to ~90% confluency in 100 mm dishes and differentiated into macrophages using phorbol 12-myristate 13-acetate (PMA). Lysosomes were isolated using a commercial isolation kit (Sigma–Aldrich, cat. no. LYSISO1) following the manufacturer's instructions with few modifications. Briefly, cells were harvested by centrifugation at 600 × g for 5 min, resuspended in 2.7 volumes of 1× extraction buffer, and homogenized using a glass Dounce homogenizer. Cell disruption was monitored by trypan blue staining until ~80–85% of cells were broken. Nuclei were removed by centrifugation at 1,000 × g for 10 min, and the post-nuclear supernatant was centrifuged at 20,000 × g for 20 min to obtain a crude lysosomal pellet. This pellet was resuspended in 0.4 mL of 1× extraction buffer per 1 × 10^8 cells. For enrichment, crude lysosomes were further purified by density gradient centrifugation on a multistep OptiPrep gradient (Sigma–Aldrich) at 150,000 × g for 4 h. Fractions (0.5 mL) were collected sequentially from the top of the gradient for downstream analysis.

Lipid Extraction from Mycobacterial Extracellular Vesicles (MEVs)

Lipids were extracted from MEVs as previously described [73], with minor modifications. Briefly, purified MEVs were washed three times with cold sterile PBS and resuspended in 1 mL PBS in a glass vial. Lipids were extracted by adding 3 mL of chloroform–methanol (2:1, v/v), followed by vortexing and centrifugation at 4,000 rpm for 10 min at 4 °C. The lower organic phase was collected, while the remaining aqueous phase was acidified with 2% formic acid and re-extracted with 2 mL chloroform to enrich phospholipids. After centrifugation under the same conditions, the organic phase was collected and pooled with the initial extract. Combined organic phases were dried under a gentle stream of nitrogen gas at room temperature and stored at –80 °C until further use. Total lipid content was quantified as previously described [74].

MDLV preparation

Estimated MEV-derived lipids were used to prepare thin lipid films in amber vials (Avanti–Sigma) for the generation of MEV-derived lipid vesicles (MDLVs). Briefly, chloroform was evaporated under a gentle nitrogen stream, followed by vacuum drying for 2 h to remove residual solvent. The resulting dry lipid films were rehydrated in 1 mL PBS (pH 7.4). MDLV preparation involved heating the suspension in a hot water bath at 80 °C and vortexing to ensure complete resuspension. The vesicles were then extruded using an Avanti® Mini Extruder through a 100 nm polycarbonate membrane with 10 mm support filters. A minimum of 25 extrusion passes was performed. Following extrusion, vesicle size distribution was confirmed using dynamic light scattering (DLS). Furthermore, the concentration was estimated using the method as mentioned earlier.

Atomic Force Spectroscopy

MFP-3D atomic force microscope (Asylum Research, Santa Barbara, CA, USA) with silicon nitride cantilevers (Oxford Instruments) and a nominal resonance frequency and a spring constant of 30 kHz and 0.16 N/m, respectively, were used for force spectroscopy experiments in contact mode. Cantilever calibration was done using the thermal noise method to obtain a spring constant of 0.10–0.19 N/m. The applied load was 1 nN, and the cantilever velocity was fixed at 6 μm/s. Differentiated THP-1 cells were incubated with MVs at ratio of 1:200 (cell: vesicles) for different time points i.e., 2, 6 and 24 h. The force curves were recorded in the region of the cell body, which was between the cell periphery and the nucleus. In each set of independent experiments, at least 100 cells were used for force spectroscopy. Igor software (Asylum Research) was used to calculate the elastic modulus by fitting the force curve using the Hertz model after providing the necessary data about the tip geometry and Poisson's ratio of the sample. For analysis of membrane tethers (tether force, tether number, and lengths), a reported custom-made MATLAB program was used.

F-actin Immunofluorescence and Actin Isosurface Imaging

Differentiated THP-1 cells were incubated with MVs at ratio of 1:200 (cell: vesicles) for different time points, i.e., 2, 6 and 24 h. Later on, cells were fixed with 4% paraformaldehyde for 10 min at RT and rinsed with 1× PBS for three times. Then, cells were permeabilized using 0.1% Triton-X-100 in 1× PBS, followed by blocking in 1% BSA for 1.5 h and rinsed with PBS/PBST. TRITC-Phalloidin was used to stain F-actin (2 μg/mL) for 30 min in the dark; it was rinsed thoroughly with 1× PBS, and slides were mounted with mounting media. Images were taken on a laser scanning confocal microscope (Olympus FV3000) using a 60×/1.4 NA objective. The 3D reconstruction of the filaments from confocal stacks was carried out with Cellsense (Evident Scientific) software. 60 to 80 cells in each set (n=2; N=3) for various conditions were analyzed. The approximate volumes enclosed by isosurfaces were normalized by the projected area of the cells, which was obtained using 3D Object Counter Fiji plugin. The significance level was assessed by One-way ANOVA using GraphPad Prism software version 10.1.0. Post-acquisition image analysis for F-actin structures was performed using the FiloQuant plugin in Fiji software. Relative quantification was

determined by calculating the number of punctae (ITCN plugin, ImageJ), filaments (FiloQuant plugin, Fiji) of F-actin per cell. Actin anisotropy was done using the Fibril Tool Fiji pluginA minimum of 120-150 cells from randomly selected fields was scored per condition.

Transcriptome profiling

RNA Extraction and Quality Assessment

Differentiated THP-1 macrophages treated with MEVs for 2 h, 12 h, or 24 h were harvested for RNA extraction. Total RNA was isolated using TRIzol Reagent (Invitrogen) according to the manufacturer's protocol. RNA concentration and purity were assessed using a NanoDrop spectrophotometer (Thermo Fisher Scientific).

Library Preparation and RNA Sequencing

RNA sequencing and library preparation were performed by Eurofins Genomics Pvt. Ltd. Libraries were generated using the TruSeq Stranded Total RNA Library Prep Kit (Illumina) with rRNA depletion. cDNA was synthesised using random primers. Paired-end sequencing libraries (2 × 150 bp) were prepared following the manufacturer’s instructions and sequenced on an Illumina platform.

RNA-seq Data Processing and Analysis

Raw reads from the samples were processed using Trimmomatic v0.39 to remove adapter sequences, ambiguous bases (>5% N), and low-quality reads (>10% bases with Phred QV < 25). Reads shorter than 100 nt after trimming were discarded. High-quality paired-end reads (QV > 25) were retained for alignment.

Reads were mapped to the Homo sapiens GRCh38 reference genome (Ensembl release 111) using STAR v2.7.10a with default parameters. Gene-level quantification was performed with featureCounts. Differential gene expression analysis was carried out using DESeq2, and functional enrichment analysis was performed using ClusterProfiler. All downstream analyses and visualisations were conducted in R.

Lipidomics analysis

Liquid Chromatography

Extracted lipids were then analysed in both positive and negative ion mode using a 1290 Infinity UHPLC System attached to a 6550 iFunnel Q-TOF system (Agilent Technologies, USA). The lipids were identified using databases available online. An Agilent 1200 HPLC (Agilent Technologies; Palo Alto, CA) with a 2.1 inner diameter (ID) × 150 mm, 3.5 µm XBridge C18 column (Waters Corp.; Milford, MA) heated to 45°C was used with a binary solvent system and a flow rate of 0.175ml/min (Sartain et al., 2011). Equilibration was performed with 95% solvent A (0.1% formic acid in filtered MilliQ water) and 5% solvent B (0.1% formic acid in acetonitrile). A 5 µL aliquot of lipid extract (equivalent to 20 µg of dried extract) was injected onto the column. The

gradient began with the initial solvent composition held for 5 minutes, followed by a 24-minute linear increase to 100% solvent B, which was then maintained for an additional 5 minutes.

Mass Spectrometry

An Agilent Mass Spectrometer Quadrupole time-of-flight (MS Q-TOF) G6545XT equipped with a Dual AJS ESI mode source was used for accurate mass analysis of the LC eluent. Positive- (+) and negative- (-) ion data were generated by operation of the mass spectrometer with a capillary voltage of 4000 V, nebulizer of 45 psig, drying gas of 8 l/min, gas temperature of 300°C, fragmentor of 175 V, charging voltage of 2000 V, skimmer of 65 V, and octopole radio frequency voltage of 750 V. Mass spectra were acquired at a rate of 1.00 spectra/s and data were collected as profiled spectra over a mass range of 100 to 3,200 Da. Mass calibration was performed with an Agilent tune mix from 100 to 3,200 Da. Data were collected with the Agilent Qualitative Analysis of MassHunter Acquisition Data software, version 10.0. Positive-ion mass spectra were acquired in Auto MS/MS mode, and collision energies with slope of 6.5 V/100 Da and offset 2.0V were used for fragmentation.

Quantification of lipids

LC/MS data files were analyzed using MassHunter Qualitative Analysis Software, version B.10.00 (Agilent Technologies, Santa Clara, CA). Molecular features (MFs) were extracted from the raw data using the Molecular Feature Extraction (MFE) algorithm, which identifies covariant ions, such as isotopes and charge states, from accurate mass LC/MS data and consolidates them into a single feature. The parameters for MFE were set to extract small molecules with a minimum peak filter of 1000 counts. Ion species were limited to +H, +Na, +NH4, +K with a peak spacing tolerance of 0.0005 m/z plus 5.0 ppm. The isotope model was configured for common organic molecules, and the charge state range was restricted to 1–2. No compound filters, mass filters, or mass defect constraints were applied. The extracted MFs were then identified using MassHunter through compound screening based on formulas obtained from the Mtb LipidDB and MycoMass databases for Mtb MV and MV fused with lysosome samples and Lipid Maps https://www.lipidmaps.org/ (mammalian lipid database) used for MV fused lysosome and only lysosome samples. The search was conducted with parameters set to match mass values only, using a match tolerance of 5 mDa with a charge state range of 1–2. From the resulting compound list, the quantitative abundance of each identified molecule was calculated using the following formula.

ppm of each lipid =

$$\frac{area\ of\ a\ lipid\ \times\ 1.25}{area\ of\ IS\ (reserpine)}$$

where, 1.25 is the ppm (concentration) of reserpine (internal standard) used.

Molarity of a lipid =

$$\frac{ppm \times 0.001}{experiment\ mass}$$

Mol% of each lipid =

$$\frac{Molarity \times 100}{Sum\ of\ molarity\ of\ total\ lipids}$$

Image & Statistical analysis

All data are representative of at least three independent experiments (n = 3), unless otherwise specified in the figure legends. Image analysis and processing were performed using ImageJ. Flow cytometry data were analysed using BD FACS DIVA (BD Biosciences, USA). Statistical significance was assessed using one-way ANOVA with Tukey`s test, with $p < 0.05$ considered significant. All statistical analyses were performed using OriginPro software and SigmaPlot.

References

1 Desjardins, M. & Griffiths, G. Phagocytosis: latex leads the way. *Current opinion in cell biology* **15**, 498-503, doi:10.1016/s0955-0674(03)00083-8 (2003).

2 Fairn, G. D. & Grinstein, S. How nascent phagosomes mature to become phagolysosomes. *Trends in immunology* **33**, 397-405, doi:10.1016/j.it.2012.03.003 (2012).

3 Niedergang, F. & Grinstein, S. How to build a phagosome: new concepts for an old process. *Current opinion in cell biology* **50**, 57-63, doi:10.1016/j.ceb.2018.01.009 (2018).

4 Roberts, E. A., Chua, J., Kyei, G. B. & Deretic, V. Higher order Rab programming in phagolysosome biogenesis. *The Journal of cell biology* **174**, 923-929, doi:10.1083/jcb.200603026 (2006).

5 Smith, A. C. *et al.* A network of Rab GTPases controls phagosome maturation and is modulated by Salmonella enterica serovar Typhimurium. *The Journal of cell biology* **176**, 263-268, doi:10.1083/jcb.200611056 (2007).

6 Husebye, H. *et al.* The Rab11a GTPase controls Toll-like receptor 4-induced activation of interferon regulatory factor-3 on phagosomes. *Immunity* **33**, 583-596, doi:10.1016/j.immuni.2010.09.010 (2010).

7 Armstrong, J. A. & Hart, P. D. Response of cultured macrophages to Mycobacterium tuberculosis, with observations on fusion of lysosomes with phagosomes. *The Journal of experimental medicine* **134**, 713-740, doi:10.1084/jem.134.3.713 (1971).

8 Smith, J. *et al.* Evidence for pore formation in host cell membranes by ESX-1-secreted ESAT-6 and its role in Mycobacterium marinum escape from the vacuole. *Infection and immunity* **76**, 5478-5487, doi:10.1128/iai.00614-08 (2008).

9 van der Wel, N. *et al.* M. tuberculosis and M. leprae translocate from the phagolysosome to the cytosol in myeloid cells. *Cell* **129**, 1287-1298, doi:10.1016/j.cell.2007.05.059 (2007).

10 Beatty, W. L. *et al.* Trafficking and release of mycobacterial lipids from infected macrophages. *Traffic (Copenhagen, Denmark)* **1**, 235-247, doi:10.1034/j.1600-0854.2000.010306.x (2000).

11 Fratti, R. A., Backer, J. M., Gruenberg, J., Corvera, S. & Deretic, V. Role of phosphatidylinositol 3-kinase and Rab5 effectors in phagosomal biogenesis and mycobacterial phagosome maturation arrest. *The Journal of cell biology* **154**, 631-644, doi:10.1083/jcb.200106049 (2001).

12 Fratti, R. A., Chua, J., Vergne, I. & Deretic, V. Mycobacterium tuberculosis glycosylated phosphatidylinositol causes phagosome maturation arrest. *Proceedings of the National Academy of Sciences of the United States of America* **100**, 5437-5442, doi:10.1073/pnas.0737613100 (2003).

13 Santamaria, C. *et al.* Trehalose dimycolate inhibits phagosome maturation and promotes intracellular M. tuberculosis growth via noncanonical SNARE interactions. *Proceedings of the National Academy of Sciences of the United States of America* **122**, e2423292122, doi:10.1073/pnas.2423292122 (2025).

14 Bach, H., Papavinasasundaram, K. G., Wong, D., Hmama, Z. & Av-Gay, Y. Mycobacterium tuberculosis virulence is mediated by PtpA dephosphorylation of human vacuolar protein sorting 33B. *Cell host & microbe* **3**, 316-322, doi:10.1016/j.chom.2008.03.008 (2008).

15 Wong, D., Bach, H., Sun, J., Hmama, Z. & Av-Gay, Y. Mycobacterium tuberculosis protein tyrosine phosphatase (PtpA) excludes host vacuolar-H+-ATPase to inhibit phagosome acidification. *Proceedings of the National Academy of Sciences of the*

United States of America **108**, 19371-19376, doi:10.1073/pnas.1109201108 (2011).
16 Sturgill-Koszycki, S. *et al.* Lack of acidification in Mycobacterium phagosomes produced by exclusion of the vesicular proton-ATPase. *Science (New York, N.Y.)* **263**, 678-681, doi:10.1126/science.8303277 (1994).
17 Philips, J. A. Mycobacterial manipulation of vacuolar sorting. *Cellular microbiology* **10**, 2408-2415, doi:10.1111/j.1462-5822.2008.01239.x (2008).
18 Gaur, R. L. *et al.* LprG-mediated surface expression of lipoarabinomannan is essential for virulence of Mycobacterium tuberculosis. *PLoS pathogens* **10**, e1004376, doi:10.1371/journal.ppat.1004376 (2014).
19 Russell, D. G. Mycobacterium tuberculosis and the intimate discourse of a chronic infection. *Immunological reviews* **240**, 252-268, doi:10.1111/j.1600-065X.2010.00984.x (2011).
20 Warner, D. F., Barczak, A. K., Gutierrez, M. G. & Mizrahi, V. Mycobacterium tuberculosis biology, pathogenicity and interaction with the host. *Nature reviews. Microbiology* **23**, 788-804, doi:10.1038/s41579-025-01201-x (2025).
21 Salgueiro, V. C. *et al.* Extracellular vesicles in mycobacteria: new findings in biogenesis, host-pathogen interactions, and diagnostics. *mBio* **15**, e0255223, doi:10.1128/mbio.02552-23 (2024).
22 Prados-Rosales, R. *et al.* Mycobacteria release active membrane vesicles that modulate immune responses in a TLR2-dependent manner in mice. *The Journal of clinical investigation* **121**, 1471-1483, doi:10.1172/jci44261 (2011).
23 Prados-Rosales, R. *et al.* Mycobacterial membrane vesicles administered systemically in mice induce a protective immune response to surface compartments of Mycobacterium tuberculosis. *mBio* **5**, e01921-01914, doi:10.1128/mBio.01921-14 (2014).
24 Athman, J. J. *et al.* Mycobacterium tuberculosis Membrane Vesicles Inhibit T Cell Activation. *Journal of immunology (Baltimore, Md. : 1950)* **198**, 2028-2037, doi:10.4049/jimmunol.1601199 (2017).
25 Mathew, L. & Kapoor, S. Methods for Studying Fusion of Bacterial Extracellular Vesicles with Intact Bacteria and Host Cells. *Methods in molecular biology (Clifton, N.J.)* **2843**, 119-136, doi:10.1007/978-1-0716-4055-5_8 (2024).
26 Rahaman, W. & Chaudhuri, A. Relative biomembrane fusogenicities of the tumor-selective liposomes of RGDK- and CGKRK-lipopeptides. *Nanoscale* **16**, 9836-9852, doi:10.1039/d4nr00450g (2024).
27 Prince, A. *et al.* Lipid Specificity of the Fusion of Bacterial Extracellular Vesicles with the Host Membrane. *The journal of physical chemistry. B* **128**, 8116-8130, doi:10.1021/acs.jpcb.4c02321 (2024).
28 Roffay, C. *et al.* Tutorial: fluorescence lifetime microscopy of membrane mechanosensitive Flipper probes. *Nature protocols* **19**, 3457-3469, doi:10.1038/s41596-024-01027-6 (2024).
29 Roffay, C. *et al.* Passive coupling of membrane tension and cell volume during active response of cells to osmosis. *Proceedings of the National Academy of Sciences of the United States of America* **118**, doi:10.1073/pnas.2103228118 (2021).
30 Chen, X. X. *et al.* Fluorogenic In Situ Thioacetalization: Expanding the Chemical Space of Fluorescent Probes, Including Unorthodox, Bifurcated, and Mechanosensitive Chalcogen Bonds. *JACS Au* **3**, 2557-2565, doi:10.1021/jacsau.3c00364 (2023).
31 Mercier, V. *et al.* Endosomal membrane tension regulates ESCRT-III-dependent intra-lumenal vesicle formation. *Nature cell biology* **22**, 947-959, doi:10.1038/s41556-020-0546-4 (2020).

32 Shi, Z., Graber, Z. T., Baumgart, T., Stone, H. A. & Cohen, A. E. Cell Membranes Resist Flow. *Cell* **175**, 1769-1779.e1713, doi:10.1016/j.cell.2018.09.054 (2018).
33 Shi, Z. & Baumgart, T. Membrane tension and peripheral protein density mediate membrane shape transitions. *Nature communications* **6**, 5974, doi:10.1038/ncomms6974 (2015).
34 Saleem, M. *et al.* A balance between membrane elasticity and polymerization energy sets the shape of spherical clathrin coats. *Nature communications* **6**, 6249, doi:10.1038/ncomms7249 (2015).
35 Zasadzinski, J. A., Viswanathan, R., Madsen, L., Garnaes, J. & Schwartz, D. K. Langmuir-Blodgett films. *Science (New York, N.Y.)* **263**, 1726-1733, doi:10.1126/science.8134836 (1994).
36 Koiri, D. *et al.* Real-time visualization reveals Mycobacterium tuberculosis ESAT-6 disrupts phagosome-like compartment via fibril-mediated vesiculation. *Cell reports* **44**, 115328, doi:10.1016/j.celrep.2025.115328 (2025).
37 Nakayama, H. *et al.* Identification of anti-lipoarabinomannan antibodies against mannan core and their effects on phagocytosis of mycobacteria by human neutrophils. *Tuberculosis (Edinburgh, Scotland)* **132**, 102165, doi:10.1016/j.tube.2022.102165 (2022).
38 McCullough, B. R., Blanchoin, L., Martiel, J. L. & De la Cruz, E. M. Cofilin increases the bending flexibility of actin filaments: implications for severing and cell mechanics. *Journal of molecular biology* **381**, 550-558, doi:10.1016/j.jmb.2008.05.055 (2008).
39 Ketel, K. *et al.* A phosphoinositide conversion mechanism for exit from endosomes. *Nature* **529**, 408-412, doi:10.1038/nature16516 (2016).
40 Ao, X., Zou, L. & Wu, Y. Regulation of autophagy by the Rab GTPase network. *Cell death and differentiation* **21**, 348-358, doi:10.1038/cdd.2013.187 (2014).
41 Bucci, C., Thomsen, P., Nicoziani, P., McCarthy, J. & van Deurs, B. Rab7: a key to lysosome biogenesis. *Molecular biology of the cell* **11**, 467-480, doi:10.1091/mbc.11.2.467 (2000).
42 Chen, Q. *et al.* Prefused lysosomes cluster on autophagosomes regulated by VAMP8. *Cell death & disease* **12**, 939, doi:10.1038/s41419-021-04243-0 (2021).
43 Pryor, P. R. *et al.* Combinatorial SNARE complexes with VAMP7 or VAMP8 define different late endocytic fusion events. *EMBO reports* **5**, 590-595, doi:10.1038/sj.embor.7400150 (2004).
44 Lees, J. A., Li, P., Kumar, N., Weisman, L. S. & Reinisch, K. M. Insights into Lysosomal PI(3,5)P(2) Homeostasis from a Structural-Biochemical Analysis of the PIKfyve Lipid Kinase Complex. *Molecular cell* **80**, 736-743.e734, doi:10.1016/j.molcel.2020.10.003 (2020).
45 Koike, S. & Jahn, R. Rab GTPases and phosphoinositides fine-tune SNAREs dependent targeting specificity of intracellular vesicle traffic. *Nature communications* **15**, 2508, doi:10.1038/s41467-024-46678-x (2024).
46 Qi, J. *et al.* MCOLN1/TRPML1 in the lysosome: a promising target for autophagy modulation in diverse diseases. *Autophagy* **20**, 1712-1722, doi:10.1080/15548627.2024.2333715 (2024).
47 Wang, J., Guo, W., Wang, Q., Yang, Y. & Sun, X. Recent advances of myotubularin-related (MTMR) protein family in cardiovascular diseases. *Frontiers in cardiovascular medicine* **11**, 1364604, doi:10.3389/fcvm.2024.1364604 (2024).
48 Vij, R. *et al.* Salmonella Typhimurium Manipulates Syntaxin 7 to Navigate Endo-Lysosomal Trafficking in Host Cells. *Traffic (Copenhagen, Denmark)* **26**, e70010, doi:10.1111/tra.70010 (2025).

49 Yang, Z. *et al.* Macro-/micro-environment-sensitive chemosensing and biological imaging. *Chemical Society reviews* **43**, 4563-4601, doi:10.1039/c4cs00051j (2014).
50 Biswas, S. *et al.* Strategic engineering of alkyl spacer length for a pH-tolerant lysosome marker and dual organelle localization. *Chemical science* **12**, 9630-9644, doi:10.1039/d1sc00542a (2021).
51 Pal, K., Dutta, T. & Koner, A. L. An Enumerated Outlook of Intracellular Micropolarity Using Solvatochromic Organic Fluorescent Probes. *ACS omega* **6**, 28-37, doi:10.1021/acsomega.0c04920 (2021).
52 Gao, P., Pan, W., Li, N. & Tang, B. Fluorescent probes for organelle-targeted bioactive species imaging. *Chemical science* **10**, 6035-6071, doi:10.1039/c9sc01652j (2019).
53 Silswal, A., Kanojiya, A. & Koner, A. L. A Fluorogenic Far Red-Emitting Molecular Viscometer for Ascertaining Lysosomal Stress in Live Cells and Caenorhabditis elegans. *Frontiers in chemistry* **10**, 840297, doi:10.3389/fchem.2022.840297 (2022).
54 Zhang, G. J., Liu, H. W., Yang, L., Zhong, Y. G. & Zheng, Y. Z. Influence of membrane physical state on the lysosomal proton permeability. *The Journal of membrane biology* **175**, 53-62, doi:10.1007/s002320001054 (2000).
55 Jia, J. *et al.* Galectin-3 Coordinates a Cellular System for Lysosomal Repair and Removal. *Developmental cell* **52**, 69-87.e68, doi:10.1016/j.devcel.2019.10.025 (2020).
56 Settembre, C. *et al.* TFEB links autophagy to lysosomal biogenesis. *Science (New York, N.Y.)* **332**, 1429-1433, doi:10.1126/science.1204592 (2011).
57 Boot, R. G. *et al.* Identification of the non-lysosomal glucosylceramidase as beta-glucosidase 2. *The Journal of biological chemistry* **282**, 1305-1312, doi:10.1074/jbc.M610544200 (2007).
58 Corcelle-Termeau, E. *et al.* Excess sphingomyelin disturbs ATG9A trafficking and autophagosome closure. *Autophagy* **12**, 833-849, doi:10.1080/15548627.2016.1159378 (2016).
59 Levental, I. & Lyman, E. Regulation of membrane protein structure and function by their lipid nano-environment. *Nature reviews. Molecular cell biology* **24**, 107-122, doi:10.1038/s41580-022-00524-4 (2023).
60 Sezgin, E., Levental, I., Mayor, S. & Eggeling, C. The mystery of membrane organization: composition, regulation and roles of lipid rafts. *Nature reviews. Molecular cell biology* **18**, 361-374, doi:10.1038/nrm.2017.16 (2017).
61 Cambier, C. J., Falkow, S. & Ramakrishnan, L. Host evasion and exploitation schemes of Mycobacterium tuberculosis. *Cell* **159**, 1497-1509, doi:10.1016/j.cell.2014.11.024 (2014).
62 Adhyapak, P., Liang, K., Duan, M. & Kapoor, S. Effect of Host Cholesterol on the Membrane Dynamics of Outer Membrane Lipids of Mycobacteria. *Chemistry, an Asian journal* **18**, e202300697, doi:10.1002/asia.202300697 (2023).
63 Srivatsav, A. T. & Kapoor, S. Biophysical Interaction Landscape of Mycobacterial Mycolic Acids and Phenolic Glycolipids with Host Macrophage Membranes. *ACS applied bio materials* **6**, 5555-5562, doi:10.1021/acsabm.3c00748 (2023).
64 Osman, M. M., Pagán, A. J., Shanahan, J. K. & Ramakrishnan, L. Mycobacterium marinum phthiocerol dimycocerosates enhance macrophage phagosomal permeabilization and membrane damage. *PloS one* **15**, e0233252, doi:10.1371/journal.pone.0233252 (2020).
65 Barelli, H. & Antonny, B. Lipid unsaturation and organelle dynamics. *Current opinion in cell biology* **41**, 25-32, doi:10.1016/j.ceb.2016.03.012 (2016).

66 Kulakowski, G. *et al.* Lipid packing defects and membrane charge control RAB GTPase recruitment. *Traffic (Copenhagen, Denmark)* **19**, 536-545, doi:10.1111/tra.12568 (2018).
67 García-Sáez, A. J., Chiantia, S. & Schwille, P. Effect of line tension on the lateral organization of lipid membranes. *The Journal of biological chemistry* **282**, 33537-33544, doi:10.1074/jbc.M706162200 (2007).
68 Sachdeva, K. *et al.* Mycobacterium tuberculosis (Mtb) lipid mediated lysosomal rewiring in infected macrophages modulates intracellular Mtb trafficking and survival. *The Journal of biological chemistry* **295**, 9192-9210, doi:10.1074/jbc.RA120.012809 (2020).
69 Shendrik, P., Golani, G., Dharan, R., Schwarz, U. S. & Sorkin, R. Membrane Tension Inhibits Lipid Mixing by Increasing the Hemifusion Stalk Energy. *ACS nano* **17**, 18942-18951, doi:10.1021/acsnano.3c04293 (2023).
70 Kozlov, M. M. & Chernomordik, L. V. Membrane tension and membrane fusion. *Current opinion in structural biology* **33**, 61-67, doi:10.1016/j.sbi.2015.07.010 (2015).
71 Berchtold, D. *et al.* Plasma membrane stress induces relocalization of Slm proteins and activation of TORC2 to promote sphingolipid synthesis. *Nature cell biology* **14**, 542-547, doi:10.1038/ncb2480 (2012).
72 Khamaru, S., Tung, K. S. & Chattopadhyay, S. Targeting Neuropilin-1 to Enhance Immunotherapy in Melanoma: Reducing Peripheral Treg-Mediated Immunosuppression and Tumour Progression. *Immunology*, doi:10.1111/imm.70072 (2025).
73 Pathak, D., Mehendale, N., Singh, S., Mallik, R. & Kamat, S. S. Lipidomics Suggests a New Role for Ceramide Synthase in Phagocytosis. *ACS chemical biology* **13**, 2280-2287, doi:10.1021/acschembio.8b00438 (2018).
74 McMahon, A., Lu, H. & Butovich, I. A. The spectrophotometric sulfo-phospho-vanillin assessment of total lipids in human meibomian gland secretions. *Lipids* **48**, 513-525, doi:10.1007/s11745-013-3755-9 (2013).

Acknowledgements

We thank Thomas Pucadyil, Sandeep Choubey and Swagata Ghatak for critical comments on the manuscript. We thank Rohan Dhiman for the kind gift of the *M. smegmatis and M. tb H37Ra strains*. We thank Apurba Koner for the JIND-Mor probe. We acknowledge all the members of the M.S. lab for their critical reading of the manuscript. MS gratefully acknowledges extramural support from the DBT–Wellcome Trust India Alliance Intermediate Fellowship (Grant IA/I/20/2/505212), the Department of Science and Technology–SERB (Grant EMR/2017/004513) and the Department of Biotechnology (DBT), Government of India (BT/PR21226/MED/122/41/2016 and BT/INF/22/SP33046/2019) and intramural funding from the Department of Atomic Energy. SK gratefully acknowledges support from the DBT–Wellcome Trust India Alliance Intermediate Fellowship (Grant IA/I/21/1/505624).

Declaration of interests

The authors declare no competing interests.

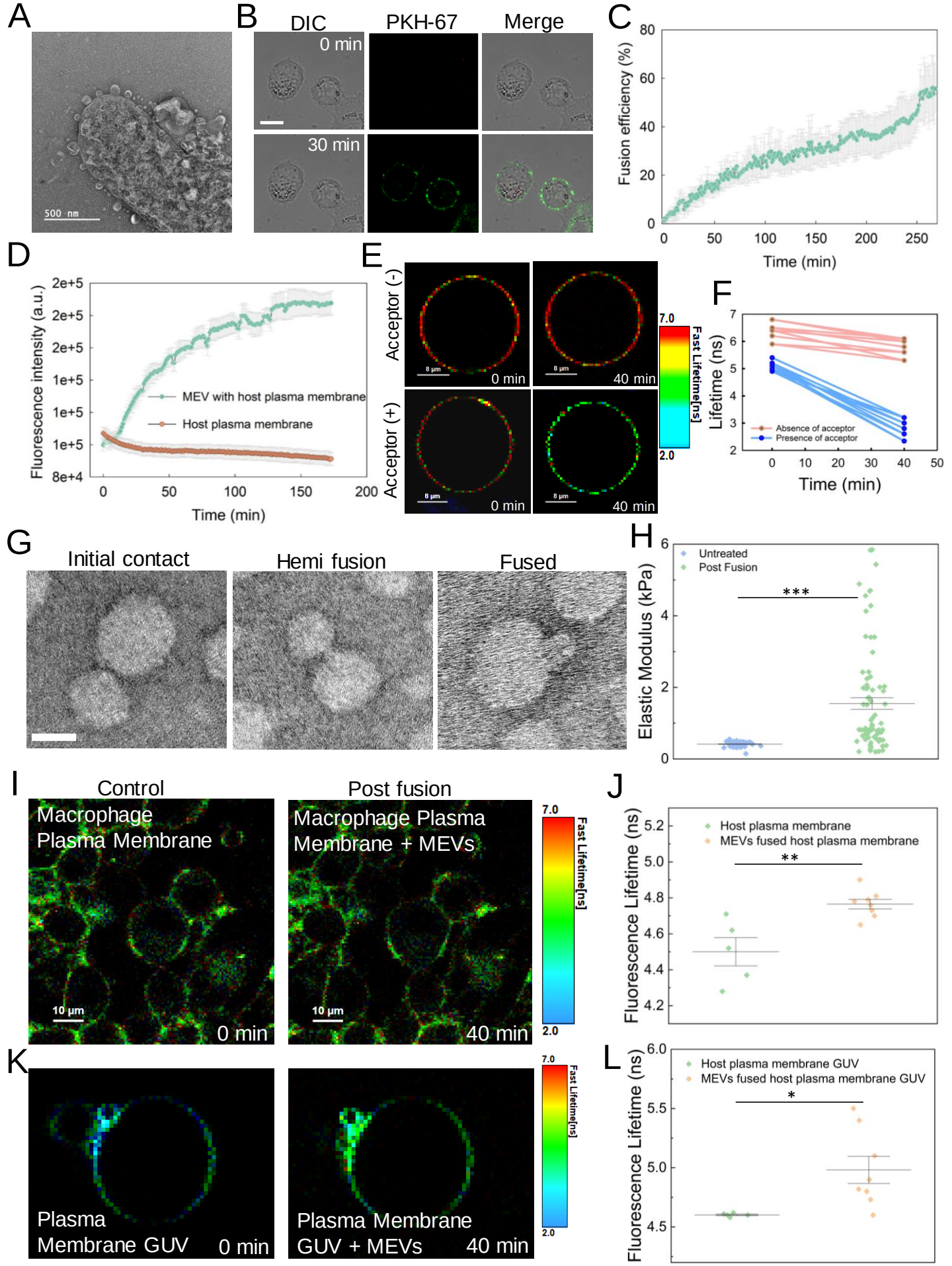
A
500 nm
B
DIC
PKH-67
Merge
0 min
30 min
C
Fusion efficiency (%)
Time (min)
D
Fluorescence intensity (a.u.)
MEV with host plasma membrane
Host plasma membrane
Time (min)
E
Acceptor (-)
Acceptor (+)
0 min
40 min
Fast Lifetime[ns]
F
Lifetime (ns)
Absence of acceptor
Presence of acceptor
Time (min)
G
Initial contact
Hemi fusion
Fused
H
Elastic Modulus (kPa)
Untreated
Post Fusion
***
I
Control
Post fusion
Macrophage Plasma Membrane
Macrophage Plasma Membrane + MEVs
10 µm
0 min
40 min
Fast Lifetime[ns]
J
Fluorescence Lifetime (ns)
Host plasma membrane
MEVs fused host plasma membrane
**
K
Plasma Membrane GUV
Plasma Membrane GUV + MEVs
0 min
40 min
Fast Lifetime[ns]
L
Fluorescence Lifetime (ns)
Host plasma membrane GUV
MEVs fused host plasma membrane GUV
*

Figure 1. Mycobacterial extracellular vesicles (MEVs) spontaneously fuse with the host plasma membrane and remodel the membrane mechanics. (a) Transmission electron micrographs representing distinct stages of mycobacterial extracellular vesicles (MEVs) formation and release from the bacterial envelope, highlighting membrane protrusion, budding, and detachment events. **(b)** Time-lapse confocal imaging of dTHP-1 macrophages incubated with PKH-67 labelled MEVs (green). Scale bar, 10µm. Images are the representative of five independent experiments (n ~250 cells). **(c)** Fusion kinetics were evaluated by monitoring the time-dependent increase in fluorescence intensity, reflecting lipid and/or content mixing between MEVs and the host plasma membrane. Nonlinear regression fits illustrate the progression of fusion over time. Data points represent mean ± S.D. from three independent experiments. **(d)** Förster resonance energy transfer (FRET) assay was performed with plasma membrane LUVs labelled with 1% NBD-PE and 1% Rh-PE. Donor fluorescence intensity was monitored as a function of time in the presence and absence of MEVs. Data points are shown as the means ± S.D. of three independent measurements. All experiments are carried out in PBS pH 7.4 at 37°C. **(e&f)** Fluorescence lifetime imaging microscopy-based Förster resonance energy transfer (FLIM-FRET) assay was performed with the plasma membrane GUV labelled with NBD-PE and the MEVs were labelled with R18. Donor Fluorescence Lifetime was monitored over a period of 40 minutes in the presence and absence of acceptor. Images are the representative of five independent experiments (n ~35 GUVs). Data points are shown from three independent experiments. All experiments are carried out in PBS pH 7.4 at 37°C. Scale bar, 8µm. **(g)** Transmission electron micrographs representing distinct stages of MEV fusion with the membrane. Scale bar, 100nm. **(h)** Mean elastic modulus values of dTHP-1 macrophage surfaces measured by atomic force microscopy (AFM) show an increase in cellular stiffness following MV fusion relative to untreated macrophages. Data are presented as mean ± SEM from ≥ 60 cells per condition. Fluorescence lifetime imaging microscopy (FLIM) analysis of membrane biophysical changes during MEV fusion. **(i)** FLIM images of Flipper-Tr labelled live macrophages before and after MEV fusion. **(j)** Quantification of Flipper-Tr fluorescence lifetimes in macrophages as shown in **(i). (k)** FLIM images of Flipper-Tr -incorporated plasma membrane–mimicking GUVs before and after exposure to MEVs. **(l)** Corresponding fluorescence lifetime measurements of GUVs as shown in **(k)**. Data points in **(j)** and **(l)** represent mean ± S.D. from each independent experiment. (**$p<0.01$, ***$p<0.001$ in one-way ANOVA).

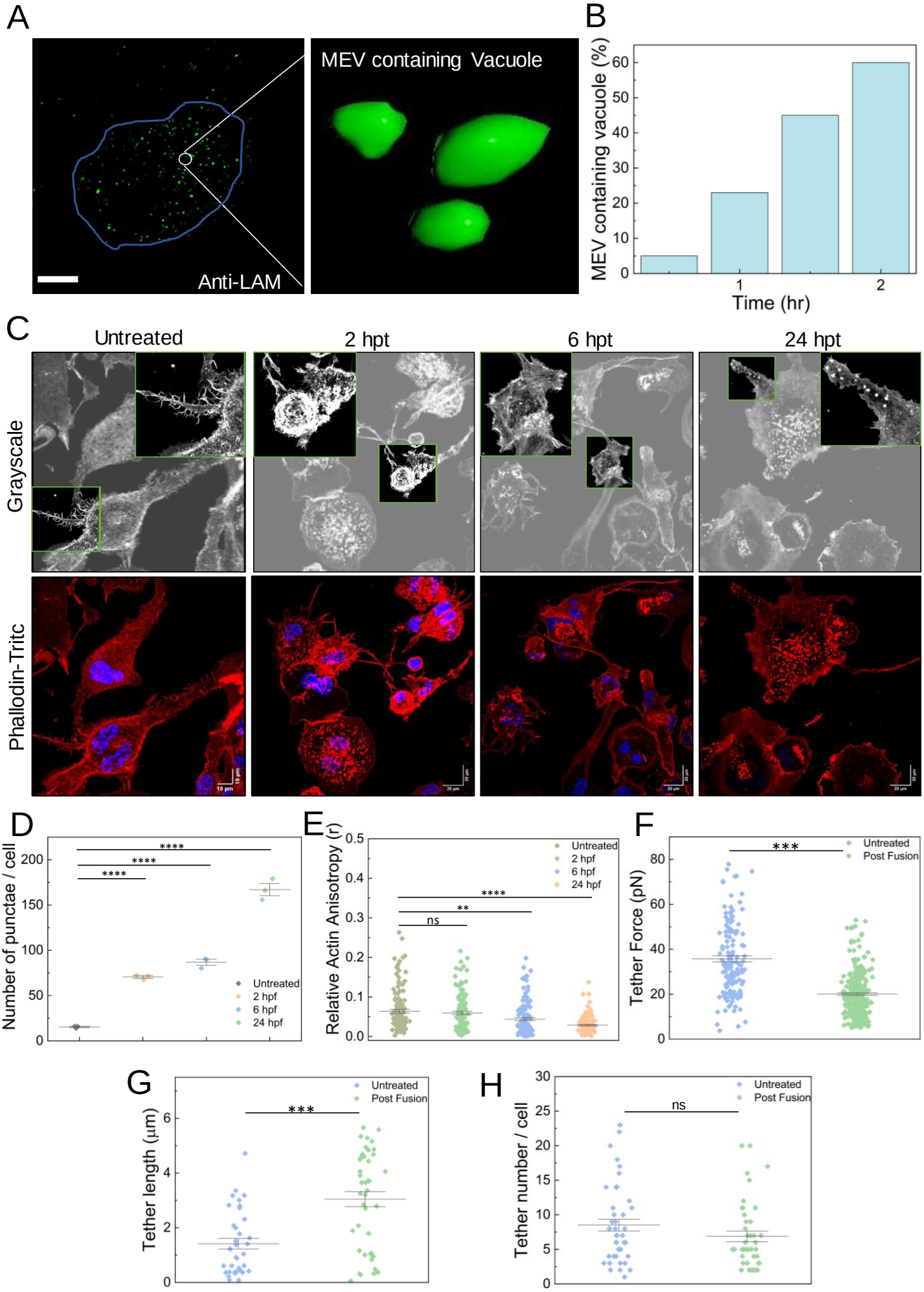
A
MEV containing Vacuole
Anti-LAM
B
MEV containing vacuole (%)
Time (hr)
C
Untreated
2 hpt
6 hpt
24 hpt
Grayscale
Phallodin-Tritc
D
Number of punctae / cell
Untreated
2 hpf
6 hpf
24 hpf
E
Relative Actin Anisotropy (r)
Untreated
2 hpf
6 hpf
24 hpf
ns
**
****
F
Tether Force (pN)
Untreated
Post Fusion
***
G
Tether length (μm)
Untreated
Post Fusion
***
H
Tether number / cell
Untreated
Post Fusion
ns

Figure 2. Temporal mapping of MEV uptake, cytoskeletal remodelling, and alterations in membrane–cortex mechanics. (a) Representative confocal micrographs showing internalized MEVs at indicated time point, detected by immunofluorescence staining using an anti-LAM antibody. **(b)** Quantification of the percentage of internalized MEVs over time, demonstrating progressive uptake by macrophages. **(c)** Representative confocal micrographs of macrophages at indicated time points following MEV treatment, showing progressive accumulation of punctate structures (red). Nuclei are stained with DAPI (blue). **(d)** Quantification of puncta per cell demonstrates a time-dependent increase upon MEV addition compared to untreated controls**. (e)** Quantitative analysis of actin anisotropy reveals misaligned actin network organisation and cytoskeletal remodelling following MEV fusion relative to control cells. Scale bars, 20 µm. Data are presented as mean ± SEM; statistical significance determined by one-way ANOVA. **(f)** Atomic force microscopy-based tether force measurements indicate altered membrane-cytoskeleton coupling in MEV-treated cells, reflected by changes in the force required to extract membrane tethers**. (g-h)** Quantification of tether length and tether number further demonstrates changes in membrane deformability and cortical tension upon MEV interaction. Data represent mean ± SEM from ~60 cells per condition. (**$p<0.01$, ***$p<0.001$ in one-way ANOVA).

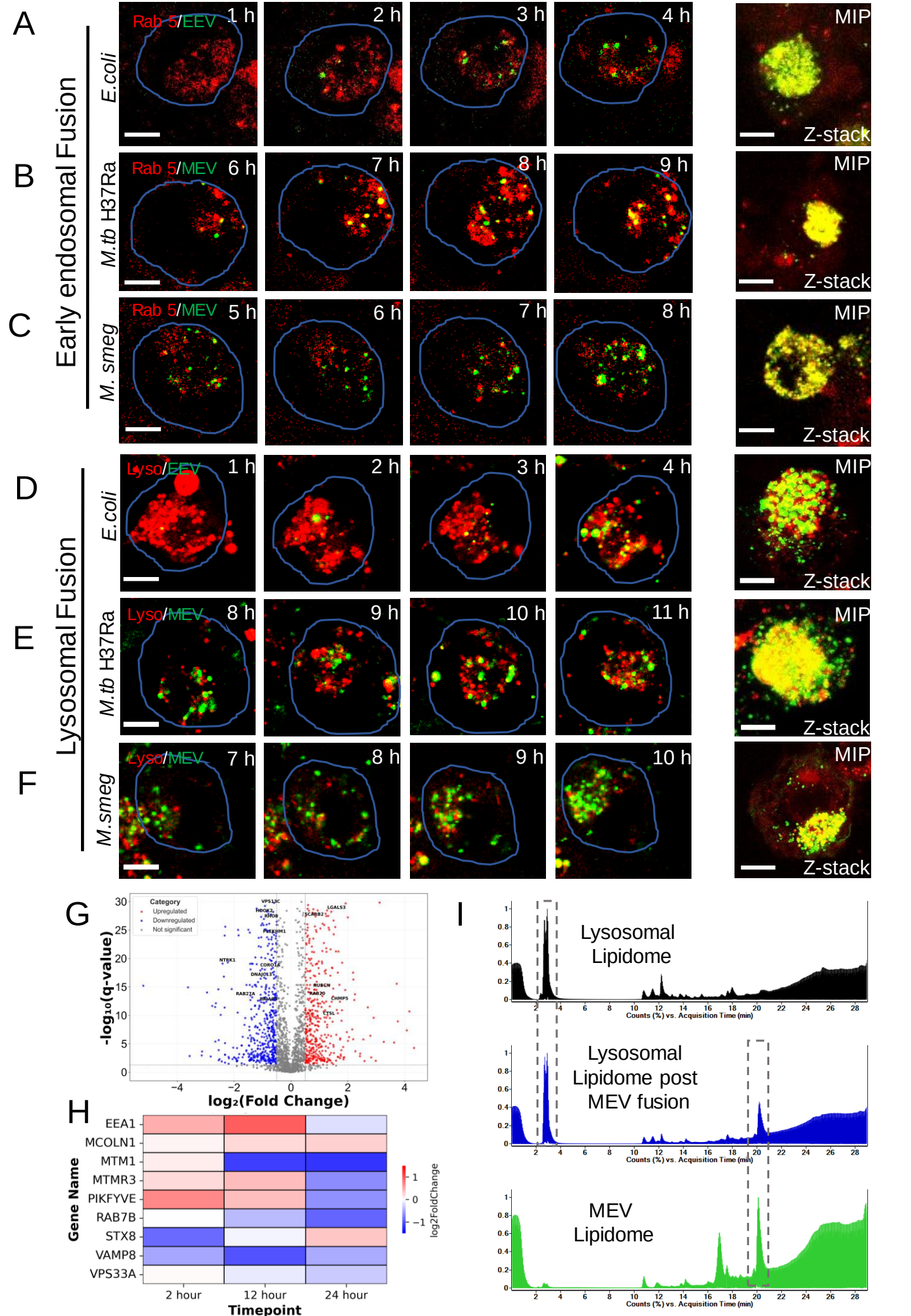
A
B
C
D
E
F
G
H
I
Early endosomal Fusion
Lysosomal Fusion
E.coli
M.tb H37Ra
M. smeg
M.smeg
Rab 5/EEV
Rab 5/MEV
Lyso/EEV
Lyso/MEV
1 h
2 h
3 h
4 h
5 h
6 h
7 h
8 h
9 h
10 h
11 h
MIP
Z-stack
Category
Upregulated
Downregulated
Not significant
-log10(q-value)
log2(Fold Change)
Gene Name
EEA1
MCOLN1
MTM1
MTMR3
PIKFYVE
RAB7B
STX8
VAMP8
VPS33A
2 hour
12 hour
24 hour
Timepoint
log2FoldChange
Lysosomal Lipidome
Lysosomal Lipidome post MEV fusion
MEV Lipidome
Counts (%) vs. Acquisition Time (min)

Figure 3. MEV fusion delays the kinetics of phagosome maturation. Live-cell time-lapse confocal imaging of early endosome-phagosome fusion following internalisation of different bacterial extracellular vesicles (Green). **(a)** *Escherichia coli* extracellular vesicles (EEVs), **(b)** *Mycobacterium tuberculosis* H37Ra extracellular vesicles (MEVs), and **(c)***Mycobacterium smegmatis* extracellular vesicles (MEVs) were internalised by macrophages stably expressing Rab5 an early endosomal marker (Red). Sequential imaging reveals dynamic fusion of Rab5-positive early endosomes with the EV-containing phagosomes. Corresponding maximum-intensity projections were acquired at the final time point from nearby cells to minimise photobleaching. The time interval between frames was 60 minutes. Scale bar, 10 µm. Each condition represents ~70 cells. Live-cell time-lapse confocal imaging of lysosome-phagosome fusion following early endosomal fusion events. **(d)** *Escherichia coli* extracellular vesicles (EEVs), **(e)** *Mycobacterium tuberculosis* H37Ra extracellular vesicles (MEVs), and **(f)** *Mycobacterium smegmatis* extracellular vesicles (MEVs) (green) were monitored for subsequent fusion with lysosomes (red). The time-series imaging demonstrates the progressive recruitment and fusion of lysosomes with EV-containing phagosomes. Maximum-intensity projections at the final time point were collected from adjacent cells to reduce photobleaching. The time interval between frames was 60 minutes. Scale bar, 10 µm. Each condition represents ~83 cells. **(g)** Volcano plot showing differentially expressed genes in macrophages 12 hours after MEV treatment. Significantly upregulated genes (n = 377, red), downregulated genes (n = 428, blue), and unchanged genes (n = 1216, grey) are indicated. **(h)** Heatmaps showing temporal gene expression profiles of macrophage genes associated with the phagosome maturation pathway at different time intervals (2,12,24 hours) following MEV treatment. **(i)** Lipidomics chromatograms comparing the lysosomal lipidome, MEV lipidome, and lysosomal lipidome following MEV fusion.

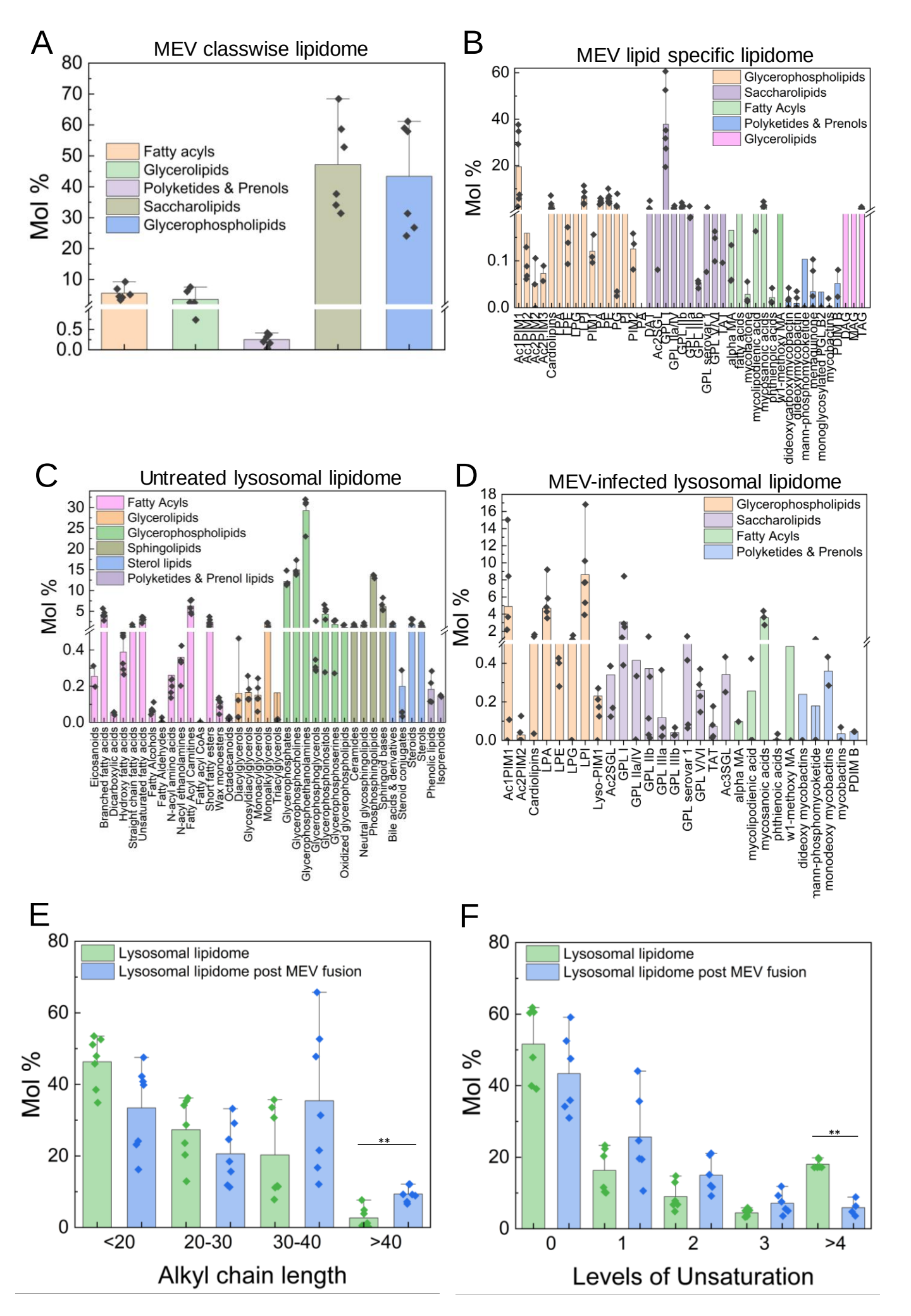
A
MEV classwise lipidome
Mol %
Fatty acyls
Glycerolipids
Polyketides & Prenols
Saccharolipids
Glycerophospholipids
B
MEV lipid specific lipidome
Mol %
Glycerophospholipids
Saccharolipids
Fatty Acyls
Polyketides & Prenols
Glycerolipids
C
Untreated lysosomal lipidome
Mol %
Fatty Acyls
Glycerolipids
Glycerophospholipids
Sphingolipids
Sterol lipids
Polyketides & Prenol lipids
Eicosanoids
Branched fatty acids
Dicarboxylic acids
Hydroxy fatty acids
Straight chain fatty acids
Unsaturated fatty acids
Fatty Alcohols
Fatty Aldehydes
N-acyl amino acids
N-acyl ethanolamines
Fatty Acyl Carnitines
Fatty acyl CoAs
Short fatty esters
Wax monoesters
Octadecanoids
Diacylglycerols
Glycosyldiacylglycerols
Monoacylglycerols
Monoalkylglycerols
Triacylglycerols
Glycerophosphates
Glycerophosphocholines
Glycerophosphoethanolamines
Glycerophosphoglycerols
Glycerophosphoinositols
Glycerophosphoserines
Oxidized glycerophospholipids
Ceramides
Neutral glycosphingolipids
Phosphosphingolipids
Sphingoid bases
Bile acids & derivatives
Steroid conjugates
Steroids
Sterols
Phenolic lipids
Isoprenoids
D
MEV-infected lysosomal lipidome
Mol %
Glycerophospholipids
Saccharolipids
Fatty Acyls
Polyketides & Prenols
Ac1PIM1
Ac2PIM2
Cardiolipins
LPA
LPE
LPG
LPI
Lyso-PIM1
Ac2SGL
GPL I
GPL IIa/IV
GPL IIb
GPL IIIa
GPL IIIb
GPL serovar 1
GPL V/VI
TAT
Ac3SGL
alpha MA
mycolipodienic acid
mycosanoic acids
phthienoic acids
w1-methoxy MA
dideoxy mycobactins
mann-phosphomycoketide
monodeoxy mycobactins
mycobactins
PDIM B
E
Lysosomal lipidome
Lysosomal lipidome post MEV fusion
Mol %
**
<20
20-30
30-40
>40
Alkyl chain length
F
Lysosomal lipidome
Lysosomal lipidome post MEV fusion
Mol %
**
0
1
2
3
>4
Levels of Unsaturation

Figure 4. Lipidomic characterisation of MEVs and MEV-fused lysosomes. reveals enrichment of MEV-derived lipids in host lysosome (a, b) Lipidomic profiling of MEVs annotated using the MtbLipidDB database. Class-wise distribution of lipid species in MEV extracts reveals a predominance of fatty acyls, followed by glycerophospholipids, saccharolipids, and additional minor lipid classes. The compositional landscape highlights the presence of *Mycobacterium*-specific lipid families, underscoring the distinct biochemical signature of MEVs derived from mycobacterial membranes. Data are presented as mean ± SEM from six independent replicates. **(c)** Class-wise lipidomic profile of untreated lysosomal lipid extracts, providing a baseline for comparison with MEV-fused lysosomes. **(d)** Lipid signatures characteristic of *Mycobacterium tuberculosis* (Mtb), identified in MEV-fused purified lysosomes and annotated using the MtbLipidDB database. Each bar represents mean lipid abundance (± SEM) from six technical replicates. The detection of Mtb-specific lipid classes in fused lysosomes indicates successful transfer and persistence of bacterial lipids within host lysosomal compartments following MEV fusion. **(e)** Distribution of acyl chain lengths and **(f)** degree of unsaturation of lipid species identified in isolated lysosomes (green) and MEV-fused lysosomal fractions (blue). Data represent mean ± SEM from six technical replicates. (**$p<0.01$, ***$p<0.001$ in one-way ANOVA).

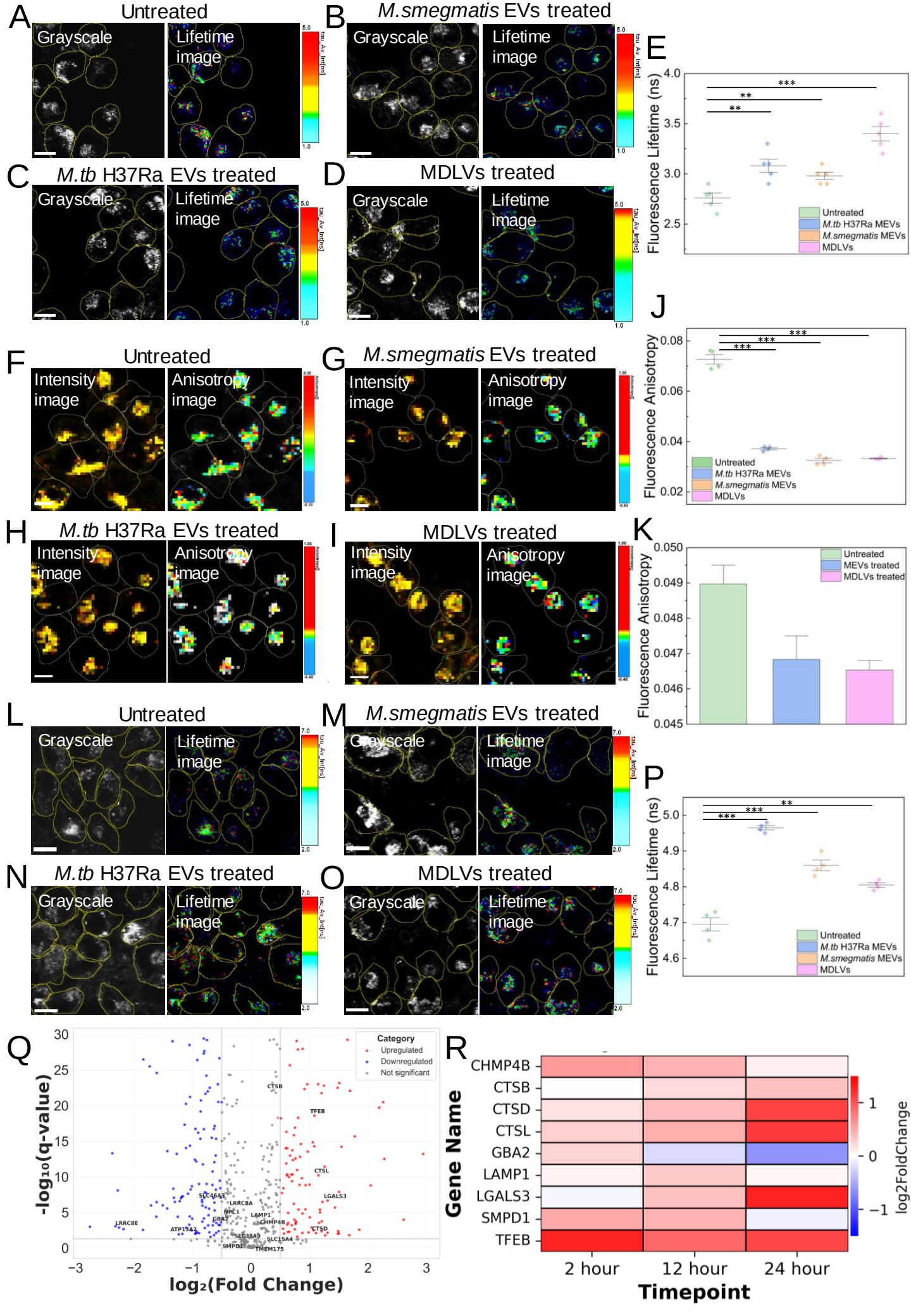
A
Untreated
Grayscale
Lifetime image
B
M.smegmatis EVs treated
Grayscale
Lifetime image
C
M.tb H37Ra EVs treated
Grayscale
Lifetime image
D
MDLVs treated
Grayscale
Lifetime image
E
Fluorescence Lifetime (ns)
Untreated
M.tb H37Ra MEVs
M.smegmatis MEVs
MDLVs
F
Untreated
Intensity image
Anisotropy image
G
M.smegmatis EVs treated
Intensity image
Anisotropy image
J
Fluorescence Anisotropy
Untreated
M.tb H37Ra MEVs
M.smegmatis MEVs
MDLVs
H
M.tb H37Ra EVs treated
Intensity image
Anisotropy image
I
MDLVs treated
Intensity image
Anisotropy image
K
Fluorescence Anisotropy
Untreated
MEVs treated
MDLVs treated
L
Untreated
Grayscale
Lifetime image
M
M.smegmatis EVs treated
Grayscale
Lifetime image
P
Fluorescence Lifetime (ns)
Untreated
M.tb H37Ra MEVs
M.smegmatis MEVs
MDLVs
N
M.tb H37Ra EVs treated
Grayscale
Lifetime image
O
MDLVs treated
Grayscale
Lifetime image
Q
Category
Upregulated
Downregulated
Not significant
-log10(q-value)
log2(Fold Change)
CTSB
TFEB
CTSL
LGALS3
CTSD
LAMP1
CHMP4B
GBA2
NPC1
LRRC8A
SLC46A3
LRRCBE
ATP13A2
SLC38A9
SLC15A4
SMPD1
TMEM175
R
Gene Name
CHMP4B
CTSB
CTSD
CTSL
GBA2
LAMP1
LGALS3
SMPD1
TFEB
2 hour
12 hour
24 hour
Timepoint
log2FoldChange

Figure 5. MEVs and MDLVs mediated disruption of lysosomal homeostasis. Fluorescence lifetime imaging microscopy (FLIM) analysis of lysosomal viscosity in macrophages treated with different MEVs. **(a)** Untreated macrophages, **(b)** *Mycobacterium smegmatis* EV–treated macrophages, **(c)** *Mycobacterium tuberculosis* H37Ra EV-treated macrophages, and **(d)** MDLV-treated macrophages stained with Jind-Mor, a lysosomal viscosity sensor. All measurements were acquired 12 hours post-treatment, revealing MEV-dependent alterations consistent with lysosomal fusion. Images are representative of five independent biological replicates (~400 cells). **(e)** Quantification of fluorescence lifetimes corresponding to the conditions shown in **(a-d).** Each data point represents the mean lifetime from an independent biological replicate. ($p < 0.05$, one-way ANOVA). FLIM analysis of lysosomal membrane anisotropy in macrophages treated with different MEVs. **(f)** Untreated macrophages, **(g)** *Mycobacterium smegmatis* EV-treated macrophages, **(h)** *Mycobacterium tuberculosis* H37Ra EV-treated macrophages, and **(i)** MDLV-treated macrophages stained with Jind-Mor. All measurements were acquired 12 hours post-treatment, revealing MEV-dependent alterations consistent with lysosomal fusion. Images are representative of five independent biological replicates (~400 cells). **(j)** Quantification of fluorescence lifetimes corresponding to the conditions shown in **(f-i).** Each data point represents the mean lifetime from an independent biological replicate. ($p < 0.05$, one-way ANOVA). **(k)** Fluorescence anisotropy measurements of isolated and purified lysosomes under different treatment conditions, untreated macrophages, *Mycobacterium tuberculosis* H37Ra EV-treated macrophages, and MDLV-treated macrophages using 1 µM DPH as a membrane-order probe. All measurements were conducted in PBS (pH 7.4) at 37 °C. The data represent three independent biological replicates. FLIM analysis of lysosomal membrane tension in macrophages treated with different MEVs. **(l)** Untreated macrophages, **(m)** *Mycobacterium smegmatis* EV-treated macrophages, **(n)** *Mycobacterium tuberculosis* H37Ra EV-treated macrophages, and **(o)** MDLV-treated macrophages stained with Lyso-Flipper, a lysosomal membrane tension sensor. All measurements were acquired 12 hours post-treatment, revealing MEV-dependent alterations consistent with lysosomal fusion. Images are representative of five independent biological replicates (~475 cells). **(p)** Quantification of fluorescence lifetimes corresponding to the conditions shown in **(l-o).** Each data point represents the mean lifetime from an independent biological replicate. ($p < 0.05$, one-way ANOVA). **(q)** Volcano plot showing differentially expressed genes in macrophages 24 hours after MEV treatment. Significantly upregulated genes (n = 90, red), downregulated genes **(**n = 106, blue), and unchanged genes (n = 282, grey) are indicated. **(r)** Heatmaps showing temporal gene expression profiles of macrophage genes associated with the Lysosomal stress at different time intervals (2,12,24 hours) following MEV treatment. (**p<0.01, ***p<0.001 in one-way ANOVA).

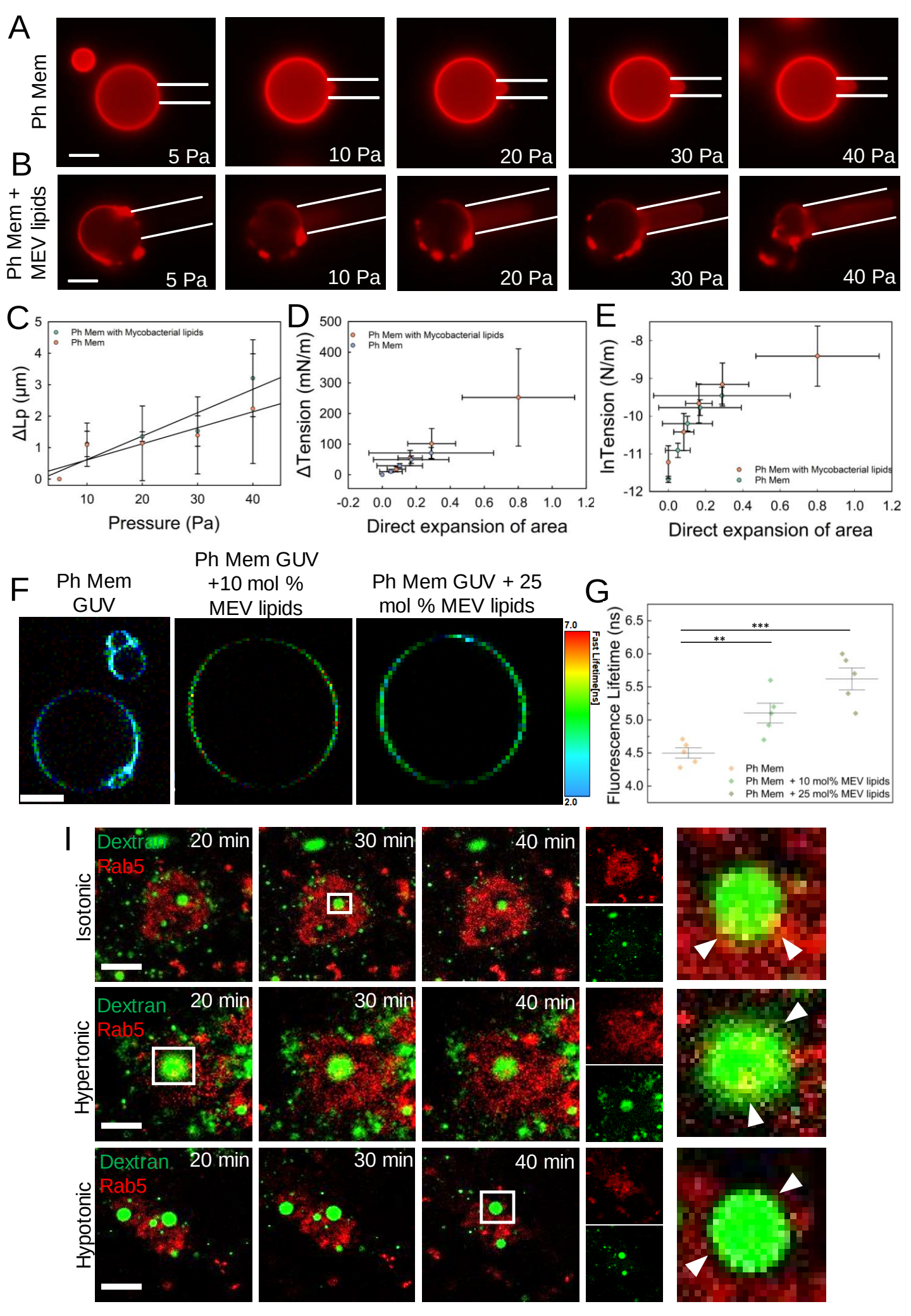
A
Ph Mem
5 Pa
10 Pa
20 Pa
30 Pa
40 Pa
B
Ph Mem + MEV lipids
5 Pa
10 Pa
20 Pa
30 Pa
40 Pa
C
Ph Mem with Mycobacterial lipids
Ph Mem
ΔLp (μm)
Pressure (Pa)
D
Ph Mem with Mycobacterial lipids
Ph Mem
ΔTension (mN/m)
Direct expansion of area
E
Ph Mem with Mycobacterial lipids
Ph Mem
lnTension (N/m)
Direct expansion of area
F
Ph Mem GUV
Ph Mem GUV +10 mol % MEV lipids
Ph Mem GUV + 25 mol % MEV lipids
7.0
2.0
Fast Lifetime[ns]
G
Fluorescence Lifetime (ns)
***
**
Ph Mem
Ph Mem + 10 mol% MEV lipids
Ph Mem + 25 mol% MEV lipids
I
Isotonic
Hypertonic
Hypotonic
Dextran
Rab5
20 min
30 min
40 min

Figure 6. MEV-derived lipids alone are sufficient to increase the phagosome membrane tension.

Time-lapse fluorescence imaging of GUVs labeled with 0.1% Rh-PE (red) during micropipette aspiration under increasing negative pressure. (**a)** Phagosomal membrane mimic and **(b)** phagosomal membrane doped with 25 mol% MEV-derived lipids. Scale bar, 5 µm. Images are representative of three independent experiments. **(c)** Plot of protrusion length (ΔL_P) versus applied pressure (P) for conditions in panels **a** and **b**. **(d)** Quantification of the area stretch modulus (K_a) derived from the relationship between change in membrane tension ($\Delta\tau$) and direct area expansion. **(e)** Quantification of the bending modulus (K_b) obtained from the semi-logarithmic plot of membrane tension versus area expansion for the conditions shown in panels **a** and **b**. Data represent mean ± SD from three independent experiments. **(f)** FLIM images of Flipper-Tr labelled phagosomal membrane mimic GUVs, Phagosomal membrane GUVs doped with 10mol% and 25mol% of MEV derived lipids. Scale bar, 5 µm. **(g)** Quantification of Flipper-Tr fluorescence lifetimes of the conditions as shown in **(f).** Each data point represents each biological replicate. All experiments are conducted in PBS (pH 7.4) at 37°C. **(i)** Time-lapse confocal imaging of macrophages stably expressing mCherry–Rab5 (red) and treated with 70-kDa fluorescent dextran (green) under different osmolarity conditions: isotonic, hypotonic (increased membrane tension), and hypertonic (reduced membrane tension). Images were acquired at 10-minute intervals. All other experimental parameters were kept identical across conditions. (**$p<0.01$, ***$p<0.001$ in one-way ANOVA).

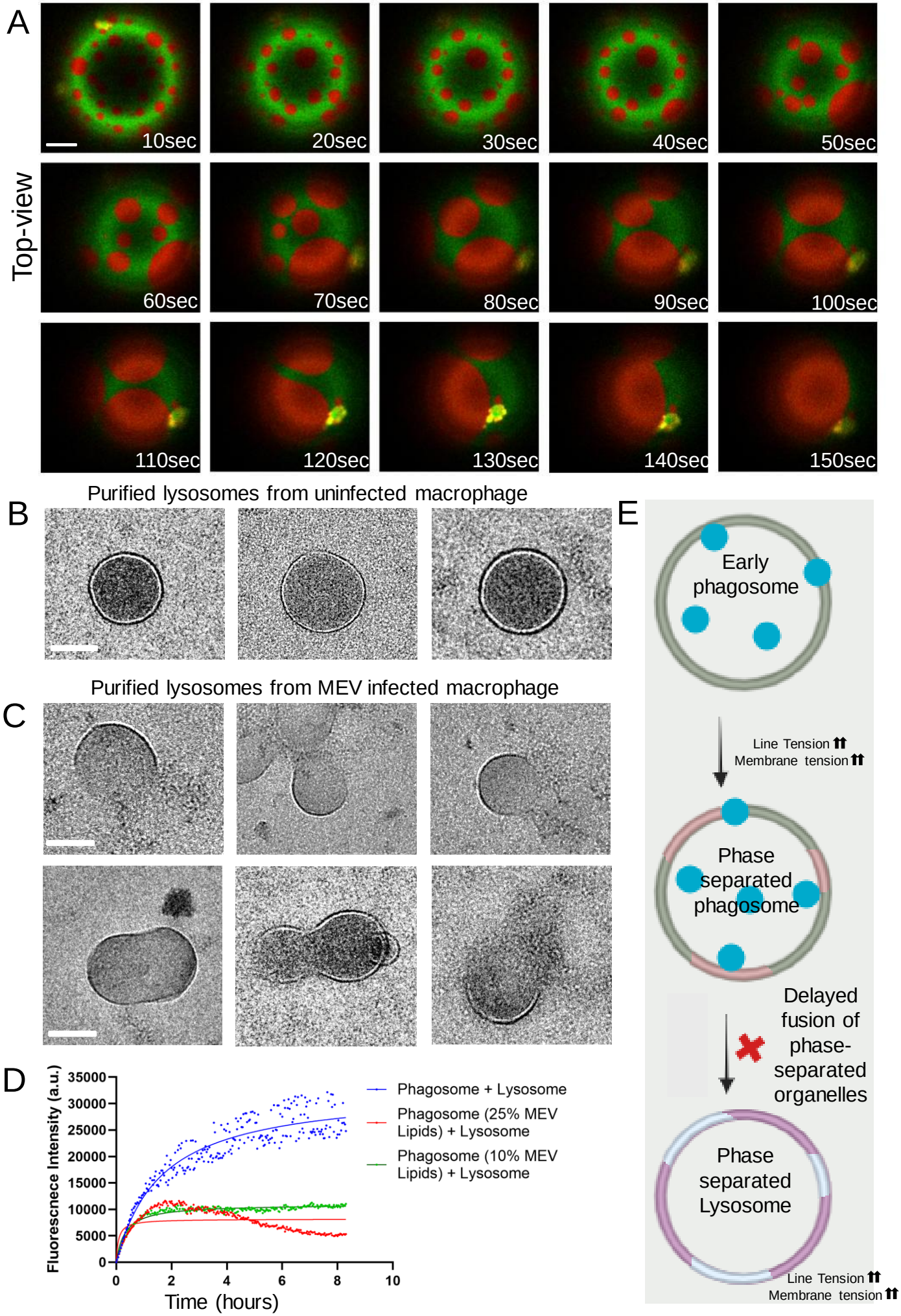
A
Top-view
10sec
20sec
30sec
40sec
50sec
60sec
70sec
80sec
90sec
100sec
110sec
120sec
130sec
140sec
150sec
B
Purified lysosomes from uninfected macrophage
C
Purified lysosomes from MEV infected macrophage
D
Fluorescnece Intensity (a.u.)
35000
30000
25000
20000
15000
10000
5000
0
0
2
4
6
8
10
Time (hours)
Phagosome + Lysosome
Phagosome (25% MEV Lipids) + Lysosome
Phagosome (10% MEV Lipids) + Lysosome
E
Early phagosome
Line Tension ⬆⬆
Membrane tension ⬆⬆
Phase separated phagosome
Delayed fusion of phase-separated organelles
Phase separated Lysosome
Line Tension ⬆⬆
Membrane tension ⬆⬆

Figure 7. Phase-separated phagosomes and lysosomes exhibit reduced fusion efficiency. (a) Time-lapse confocal imaging of phagosomal membrane–mimicking GUVs doped with 25 mol% MEV-derived lipids and labelled with 0.01% Rh-PE (red) and 0.01% TopFluor-Cholesterol (green). Images illustrate the emergence of lipid phase separation upon MEV lipid incorporation. Representative frames from five independent biological replicates are shown. All experiments were performed in PBS (pH 7.4) at 37 °C. Scale bar, 5 µm. Transmission electron micrographs of negatively stained isolated lysosomes from **(b)** uninfected macrophages and **(c)** MEV-treated macrophages. Images illustrate the morphological differences and membrane organization induced upon MEV exposure. Scale bar, 50 nm. **(d)** Förster resonance energy transfer (FRET) assay was performed with lysosomal membrane LUVs labelled with 1% NBD-PE and 1% Rh-PE. Donor fluorescence intensity was monitored as a function of time in the presence of increasing concentrations of MEV lipids. Data points are shown as the means ± S.D. of three independent measurements. All experiments are carried out in PBS pH 7.4 at 37°C. **(e)** Schematic representation illustrating how MEV-driven lipid phase separation increases membrane tension and line tension in phagosomal and lysosomal membranes, thereby inhibiting efficient phagosome–lysosome fusion.

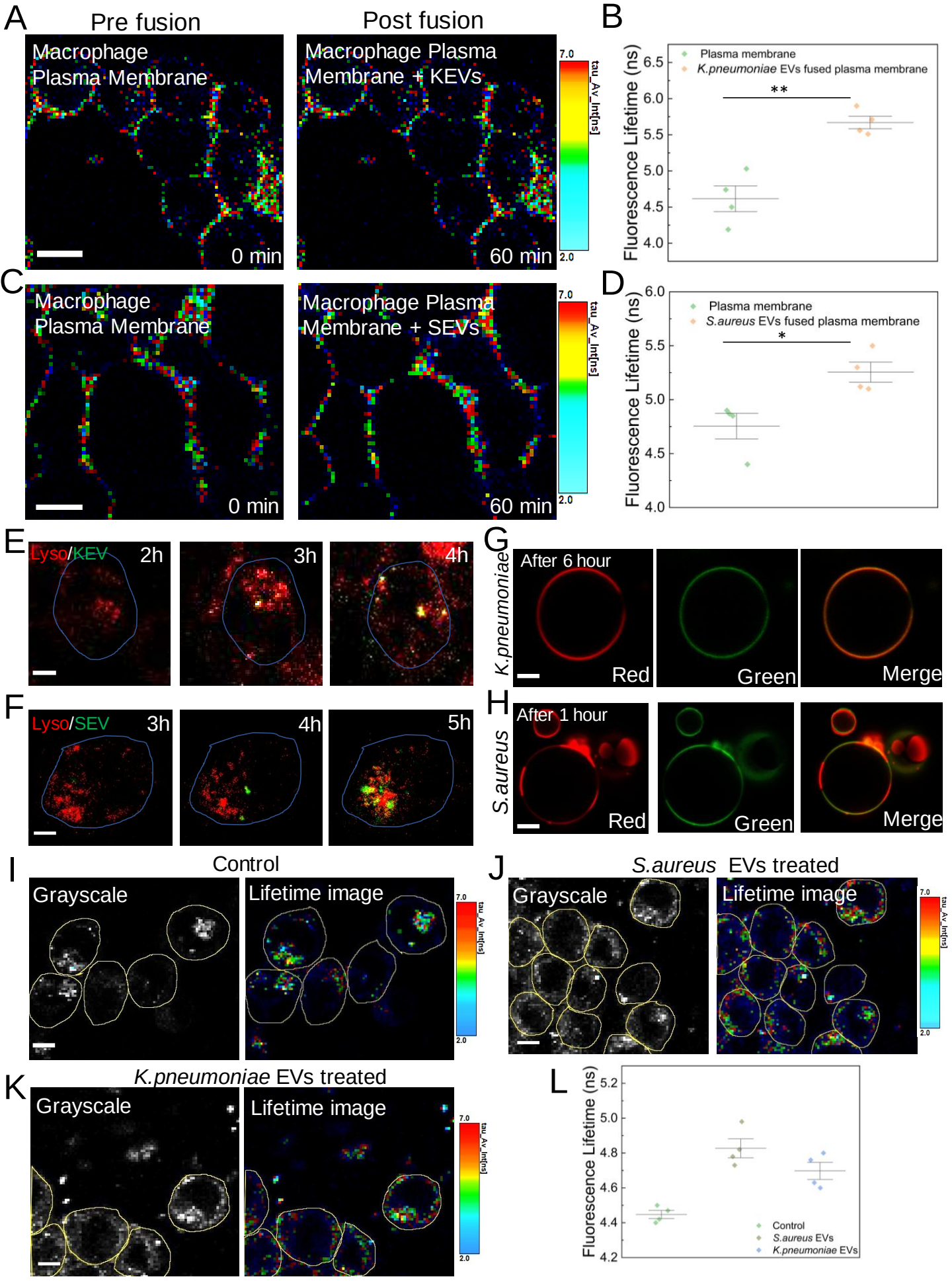
A
Pre fusion
Post fusion
Macrophage Plasma Membrane
Macrophage Plasma Membrane + KEVs
0 min
60 min
7.0
2.0
tau_Av_Int[ns]
B
Plasma membrane
K.pneumoniae EVs fused plasma membrane
**
Fluorescence Lifetime (ns)
6.5
6.0
5.5
5.0
4.5
4.0
C
Macrophage Plasma Membrane
Macrophage Plasma Membrane + SEVs
0 min
60 min
7.0
2.0
tau_Av_Int[ns]
D
Plasma membrane
S.aureus EVs fused plasma membrane
*
Fluorescence Lifetime (ns)
6.0
5.5
5.0
4.5
4.0
E
Lyso/KEV
2h
3h
4h
F
Lyso/SEV
3h
4h
5h
G
K.pneumoniae
After 6 hour
Red
Green
Merge
H
S.aureus
After 1 hour
Red
Green
Merge
I
Control
Grayscale
Lifetime image
7.0
2.0
tau_Av_Int[ns]
J
S.aureus EVs treated
Grayscale
Lifetime image
7.0
2.0
tau_Av_Int[ns]
K
K.pneumoniae EVs treated
Grayscale
Lifetime image
7.0
2.0
tau_Av_Int[ns]
L
Fluorescence Lifetime (ns)
5.2
5.0
4.8
4.6
4.4
4.2
Control
S.aureus EVs
K.pneumoniae EVs

Figure 8. Bacterial extracellular vesicles induced alterations in membrane tension and lipid organisation during phagosome maturation. Fluorescence lifetime imaging microscopy (FLIM) analysis of membrane biophysical changes during KEV and SEV fusion. **(a)** FLIM images of Flipper-Tr labelled live macrophages before and after KEV fusion. **(b)** Quantification of Flipper-Tr fluorescence lifetimes in macrophages as shown in **(a). (c)**FLIM images of Flipper-Tr labelled live macrophages before and after SEV fusion. **(d)** Quantification of Flipper-Tr fluorescence lifetimes in macrophages as shown in **(c).** Data points in **(b)** and **(d)** represent mean ± S.D. from each independent experiment. Live-cell time-lapse confocal imaging of lysosome-phagosome fusion following early endosomal fusion events. **(e)** *Klebsiella pneumoniae* extracellular vesicles (KEVs), and **(f)** *Staphylococcus aureus* extracellular vesicles (SEVs) (green) were monitored for subsequent fusion with lysosomes (red). The time-series imaging demonstrates the progressive recruitment and fusion of lysosomes with EV-containing phagosomes. The time interval between frames was 60 minutes. Scale bar, 10 µm. Each condition represents ~50 cells. Time-lapse confocal imaging of phagosomal membrane–mimicking GUVs incorporating EV-derived lipids.GUVs doped with 25 mol% EV-derived lipids and labeled with 0.01% Rh-PE (red) and 0.01% TopFluor–cholesterol (green) were imaged over time to assess lipid organization. **(g)** KEV-derived lipids and **(h)** SEV-derived lipids. Images demonstrate the emergence of lipid phase separation following EV lipid incorporation. Representative frames from five independent biological replicates are shown. All experiments were performed in PBS (pH 7.4) at 37 °C. Scale bar: 5 µm. FLIM analysis of lysosomal membrane tension in macrophages following treatment with bacterial extracellular vesicles.**(i)** Untreated macrophages, **(j)** Staphylococcus aureus EV–treated macrophages, and **(k)** Klebsiella pneumoniae EV–treated macrophages stained with Lyso-Flipper, a lysosomal membrane tension sensor. All measurements were acquired after vesicle–lysosome fusion, revealing EV-dependent alterations in lysosomal membrane tension. Images are representative of five independent biological replicates (~150 cells per condition**).(l)** Quantification of Lyso-Flipper fluorescence lifetimes corresponding to the conditions shown in (**i–k**). Each data point represents the mean lifetime from an independent biological replicate.
(**p<0.01, ***p<0.001 in one-way ANOVA).

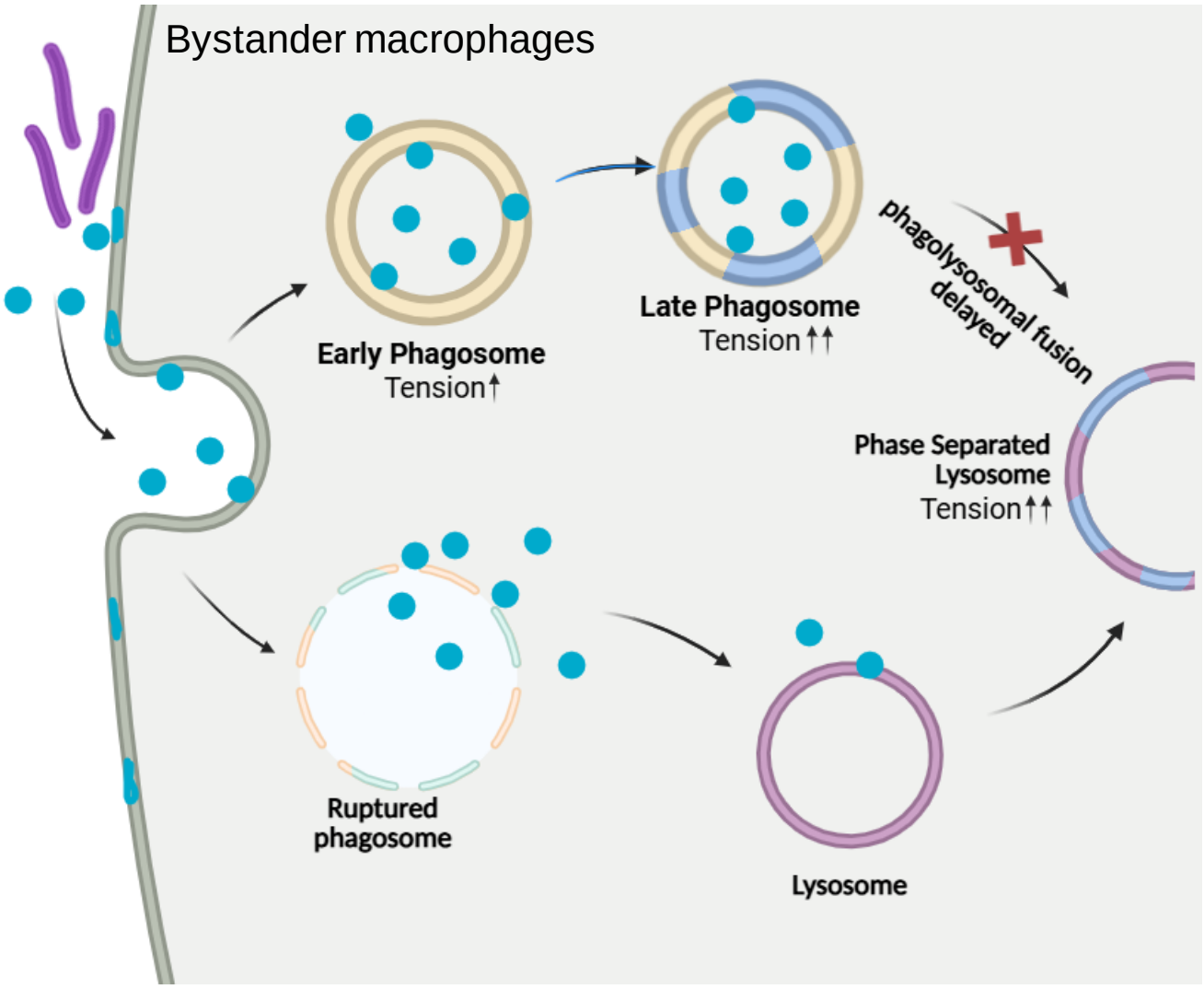
Bystander macrophages
Early Phagosome
Tension↑
Late Phagosome
Tension↑↑
phagolysosomal fusion
delayed
Phase Separated
Lysosome
Tension↑↑
Ruptured
phagosome
Lysosome

Figure 9. Schematic representation of the proposed mechanism by which MEVs mediate abortion or delay of the phagosomal maturation process in bystander macrophages.